

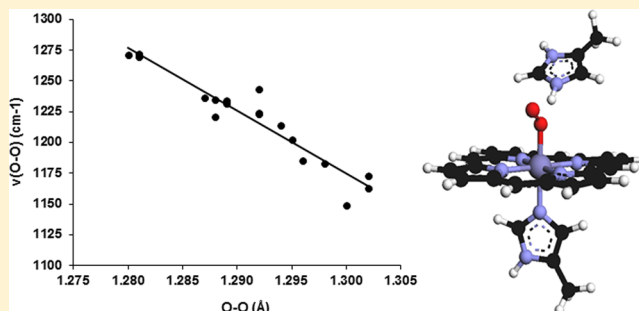
Effect of Distal Interactions on O₂ Binding to Heme

Kasper P. Kepp* and Pouria Dasmeh

DTU Chemistry, Technical University of Denmark, DK-2800 Kongens Lyngby, Denmark

Supporting Information

ABSTRACT: This paper reports DFT-computed electronic ground states, Mössbauer isomer shifts, O–O and Fe–O vibration frequencies, and thermodynamics of O₂ binding of heme models representing different distal (position E7) interactions, strictly validated against experimental data. Based on the results, the impact of specific types of distal interactions on oxyheme electronic structure can be systematized. Hydrogen bonding increases back-donation, O–O bond activation, and oxygen binding affinity. The heme side chains reduce isomer shifts by -0.06 mm/s due to electron withdrawal from iron, and distal hydrogen bonds can further reduce isomer shifts up to 0.07 mm/s. The O–O stretch vibration, the O–O distance, and the isomer shift possess substantial heuristic value in interpreting electronic structure, whereas other properties are less effective, based on computed correlation coefficients. Shorter Fe–O bond length does not correlate with O₂ affinity, as hydrogen bonding elongates both Fe–O and O–O bonds by ~ 0.01 – 0.02 Å, contrary to the situation absent from distal hydrogen bonds and of potential relevance to ligand activation where distal interactions are involved. An ionic (Weiss-type) model of Fe–O bonding combined with electron withdrawal by hydrogen bonds is shown to robustly explain the structural, spectroscopic, and thermodynamic properties of the hemes. The identified correlations may be useful, e.g., for designing O₂-activating catalysts or for diagnosing heme protein variants.



INTRODUCTION

Heme is one of the most formidable examples of molecular evolution: a highly specialized ligand system tuned to work in the electron-transfer and O₂-managing world of oxidative metabolism. Notable for this evolution is heme's ability to incorporate iron in oxidation states II, III, and IV, and much focus has been on the tuning of redox potentials^{1–7} and the evolution of small reorganization energies via the porphyrin and axial ligands associated with it.^{8,9}

Many research groups have investigated the enigmatic heme–O₂ system, notably in the past 15 years using density functional theory (DFT),^{6,10–22} and a substantial interest in correlating heme electronic structure to vibrational modes has been seen.^{23–25} An exquisite ability to incorporate Fe(II) and Fe(III) in both high- and low-spin states was identified as due to a cavity size intermediate between the ionic radii of high- and low-spin iron(II),^{8,26} further tuned by modulation of the ligand field strength of the proximal histidine by partial deprotonation.²⁷ The suggested rationale for the close-lying spin states of deoxyheme and oxyheme is to enable fast and reversible spin crossover during O₂ binding, since in the simple Landau–Zener picture^{28,29} this crossover is strongly accelerated by the near-parallel energy curves resulting from close-lying deoxy spin states.³⁰

The distal E7 site (corresponding to residue 64 in mammalian myoglobin and hemoglobin) has histidine (His) in most wild-type globins including hemoglobin (Hb) and myoglobin (Mb). This His increases the oxygenation constant

K_{O_2} by ~ 1000 -fold as is evident from E7 mutants^{31,32} and from synthetic porphines lacking the distal residue.³³ While the effect of the distal hydrogen bonding has been investigated theoretically for the wild-type His model,^{12,13,17,34} and experimentally by site-directed mutagenesis,³² a systematic understanding of the impact of distal interactions on the hemeO₂ electronic structure and their relation to spectroscopic data and O₂ binding is so far missing.³⁵ Also, theory has so far been unable to obtain accurate Fe–O₂ binding energies even for the contribution of the protein,^{12,17,20} estimated from dissociation barriers of protoheme vs myoglobin to be ~ 15 kJ/mol.^{12,31,32}

This paper reports DFT computations of a number of relevant heme models with variable distal interactions, to investigate their role in modulating the electronic structure of oxyheme. We applied both the hybrid B3LYP and metahybrid TPSSH functionals, the latter because it has been found highly accurate for modeling spin crossover^{36,37} and bond dissociation energies of metal–ligand bonds.^{38–41} We also included dispersion corrections that should provide new accuracy to these interactions, as some of them are hydrogen-bond dominated whereas others are more steric. We systematized the effect of various distal interactions on electronic structure and bonding of the oxyheme systems, including their effect on Fe–

Received: January 9, 2013

Revised: March 14, 2013

Published: March 14, 2013

to-O₂ back-bonding, Fe–O and O–O bond lengths, Mössbauer isomer shifts, O–O and Fe–O vibrations, and oxygen binding affinities. The results are in their interpretation fully consistent with previous studies on the wild-type electronic structure,¹³ and we furthermore provide the first, systematic picture of how heme electronic structure and O₂ binding are affected by changes in such distal interactions and how these changes correlate directly with spectroscopic data.

■ COMPUTATIONAL DETAILS

Choice of Density Functionals. DFT is the dominating electronic structure method for medium-sized systems.^{42–46} B3LYP^{47,48} is the most widely used functional today, although modern functionals have now entered the arena in force.⁴⁹ The amount of exact exchange was optimized to be ca. 20% in B3LYP.⁴⁷ Modern functionals, notably OLYP,^{50,51} B2PLYP,⁵² and TPSSH,^{53,54} are current contenders as the most accurate methods for use in larger molecular systems and also in cases where static correlation is massive.⁴⁹

In transition metal reactions, Fermi (exchange) correlations between same spins often change, as do the ionic and covalent components of metal–ligand bonds. Nonhybrid generalized gradient approximation (GGA) functionals such as BP86^{55,56} tend to produce too-compact electron densities, favoring tight associations, low-spin, covalent bonding, etc.⁴⁹ Hybrid functionals produce polarized, looser densities that favor open-shell parallel-spin configurations in proportion to their Hartree–Fock (HF) exchange fraction and to the number of exchange integrals. When spin quantum numbers change, B3LYP is thus biased toward high-spin configurations that are favored by HF exchange.^{57–60} B3LYP underestimates metal–ligand bond strengths across the d-block, whereas nonhybrids overestimate metal–ligand binding⁶¹ and stabilize low-spin states too much.^{36,37} B3LYP's bias toward high-spin and underbinding is also seen in porphyrins,^{26,37} and it results from the production of loose, polarized (more atomic) electron densities by HF exchange,⁴⁹ as seen also from the systematically larger B3LYP-computed dipole moments of M–L diatomics.⁶¹

The almost nonempirical TPSSH functional⁵³ with 10% exact exchange (the only fitted parameter) fulfills a number of exact constraints and performs similarly to B3LYP for the G3/99 set⁶² but is more accurate than B3LYP for various inorganic test reactions.^{38,39} For studying O₂ binding to heme, TPSSH was the most accurate functional tested for metal–ligand binding in more than 100 diatomics.^{40,41} Consistent with its balance between atomic and bound states, although M05 overall performed better in a coordinately saturated test set, TPSSH displayed the smallest signed error for bond energies.³⁹ TPSSH also gives an unprecedented small MAE of 11 kJ/mol for spin crossover enthalpies³⁶ and, relevant to heme, excellent performance for spin splitting³⁷ and geometries⁶³ of iron porphyrins. Its performance is further supported by several benchmarks that actually claimed the opposite when electronic energies were used as proxies for observed ground states, i.e., neglecting entropy.^{64,65} Since high spin is entropy-favored by typically 10–30 kJ/mol at room temperature^{66,67} due to the weaker metal–ligand bonds and thus larger vibrational entropy of high-spin systems,⁴⁹ correcting such benchmarks for entropy tend to make hybrids with large HF-exchange components (B3LYP, B2PLYP) less accurate, as HF exchange compensates neglect of entropy. Correcting for entropy, TPSSH is the best performing functional also in these cases,^{37,49} in line with quantitative benchmarks against spin crossover enthalpies

where entropy effects are zero.³⁶ It is also comforting that benchmarks of diatomics (with negligible errors from entropy, solvation, and dispersion)^{40,41,61} and of coordinately saturated systems^{36–38,40,49} are consistent when these errors are corrected for, as a physically consistent (potentially universal) functional should be accurate in both limits. In coordinately saturated complexes, the density of states is higher and, thus, errors are downscaled so that quantitative errors are often smaller while qualitative predictions are often more difficult. The performance of TPSSH for inorganic open-shell chemistry has also recently been observed in studies other than those mentioned above.^{68–70}

Applying both B3LYP and a GGA functional such as BP86 may help in estimating the spread of possible energetics obtainable from DFT, as they often produce bond-breaking and spin crossover energies on separate sides of the experimental values (TPSSH typically falls between these two due to HF exchange of 0, 20, and 10% in BP86, B3LYP, and TPSSH, respectively).^{36,40,41} Also, it is today state-of-the-art to include a semiquantitative estimate of dispersion via corrections such as DFT-D3,⁷¹ which has also been performed in this work via the implementation in Turbomole 6.3. By calculating D3 corrections with both B3LYP and TPSSH, it was validated that there were no pathological cases of distance dependence affecting the dispersion calculations, as have been first observed for some sterically crowded phenylporphyrin systems³⁷ and later confirmed also in the study of gold systems.⁷² It has also been shown previously²² that the tendency of B3LYP to underbind O₂ to heme is largely remedied by dispersion corrections, which generally favor more compact electron densities, including low-spin and bound states in bond-breaking reactions.⁴⁹

Optimizing the Electronic Configurations. All calculations were performed with the Turbomole 6.3 software,⁷³ using the Cosmo solvation model⁷⁴ with a dielectric constant of 10 to mimic a realistic condensed phase screening effect. Sensitivity to the use of screening was evaluated by computing also energies without solvation and with a dielectric constant of 4. Unrestricted calculations were performed in all cases. Open-shell singlet configurations with spin polarization on Fe and O₂ were obtained to honor the Kohn–Sham principle, as these configurations are realistic probes of the real electronic structure.⁴⁹ To illustrate this, the closed-shell singlet without any spin polarization was computed to be 59 kJ/mol above the ground state configuration for the wild-type hemeO₂ adduct with E7-His, and the use of such closed-shell singlets would thus underestimate O₂-binding energies by a similar amount. Efficient configuration optimization was achieved by first converging the $M_S = 3$ configurations and then using the optimized orbitals as input for the open-shell singlets by “spin-down coupling”, i.e., inverting α electrons to β electrons before recalculation. This procedure leads to the fully spin-polarized electronic configuration that correctly mimics in a Kohn–Sham sense the true electronic ground state of the system.

Geometry Optimization. Optimization of all geometries, both for the iron complexes used for calibrating Mössbauer isomer shifts and for the heme models, were performed at the BP86/def2-SVP level using Cosmo with a dielectric screening of 10.⁷⁵ Electronic energies were converged down to 10^{−7} hartree, and to achieve stable equilibrium geometries, the gradient was converged down to 10^{−3} au. The model complexes used for calibration of isomer shifts are described in the

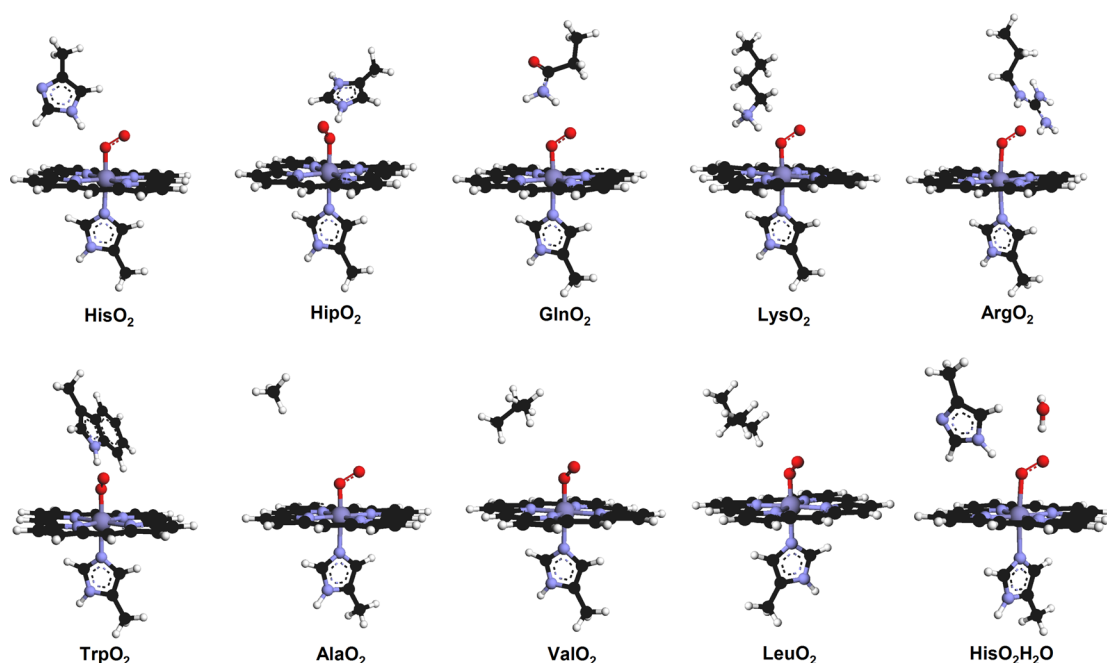


Figure 1. Examples of the general classes of oxyheme models studied in this work. The first nine show models without water, and the last is an example of a hydrated model. In addition, all water-bound combinations and the corresponding deoxy models were studied (see Supporting Information for details).

Supporting Information, and these were also geometry optimized by the same procedure.

The heme models were built from the atomic resolution structure of oxyMb at 1.0 Å resolution (PDB code 1A6M)⁷⁶ and modified according to the distal environment using ArgusLab.⁷⁷ The α carbon was changed into a hydrogen and fixed in all geometry optimizations to avoid drifting and inconsistent conformations of the systems. Heme systems of the type depicted in Figure 1 were geometry optimized before their energies and thermodynamics of O₂ binding were computed. All spin states were fully geometry optimized. All combinations of the following models were geometry optimized: open-shell singlet oxyhememes, quintet deoxy states, and water-bound models with E7-His (corresponding to wild type), Hip (protonated histidine), Gln, Lys, Arg, Trp, Ala, Val, and Leu. These models were chosen because they should reflect the range of possible distal interactions affecting O₂ binding and spectroscopic properties, including the possibility of water residing in some cases in the distal pocket,⁷⁸ and because of data available from site-directed mutagenesis.

Single-Point Energies and Free Energies. For accurate energies, we used TPSSh but also computed energies with B3LYP for comparison, with and without dispersion and scalar-relativistic energy corrections, and with a dielectric constant of either 10 or 4. For all energies, the def2-TZVPP basis set was applied.⁷⁹ A larger QZVPP basis set performs marginally better for metal–ligand bond dissociation energies, giving a 1 kJ/mol smaller root-mean-square error.⁶¹ Zero-point energies (ZPE) and enthalpy and entropy corrections were calculated from calculated harmonic frequencies and thermodynamic analysis using freeh script available with Turbomole. No scale factors were applied as BP86 has optimal vibration scale factors very close to unity (0.996) for the studied type of fundamental vibrations.⁸⁰

Calculation of Mössbauer Isomer Shifts. Whereas quadrupole splitting is a very sensitive and useful property,

for the electronic structure of interest here (the amount of charge transfer between iron and oxygen relating to, e.g., the Weiss/Pauling concepts), the isomer shift is a key property, which, as will be shown, can be understood from the way electron density on iron anticorrelates with the amount of back-donation, i.e., the Weiss character. Quadrupole splitting is not a good proxy for this aspect, as it mainly probes the heterogeneity around the iron (the angular electron density distribution), not the total electron density distribution that is relevant to back-bonding, and it is also very sensitive to the occupation of d_{xz} vs d_{yz} orbitals, with errors of >0.3 mm/s and sign inversions being common.⁸¹

The procedure for computing Mössbauer isomer shifts of iron complexes using electronic structure methods has been described in detail in the literature.^{82–88} The procedure rests on the near proportionality between changes in the electron density at the iron nucleus due to excitation and the measured isomer shift, which is caused by the changing electrostatic interaction with the electron density of the excited and ground states of the nucleus, due to their different radii.^{89,90}

Single point energies for obtaining accurate electron densities at the iron nuclei were computed at the Cosmo-optimized geometries using the def2-TZVPP basis set.⁷⁵ These energies were converged to 10^{−7} au. Using a calibration set of 20 iron complexes with known isomer shifts,^{82,91–100} a best linear regression fit was obtained, and the regression equations were subsequently used to compute the isomer shifts of the studied heme systems. For calibration, we tested the density functionals B3LYP, BP86, TPSSh, PBE, and PBE0, to estimate the spread in reproduction of the isomer shifts due to functional choice.

At higher temperature, the isomer shift (δ) decreases with temperature due to the second-order Doppler shift,¹⁰¹ with typical examples being a decrease in δ of 0.03 mm/s per 100 K.¹⁰² Thus, a good calibration fit requires experimental data at the same temperature, or otherwise corrected by a simple relation such as the above-mentioned one. When possible, the

data used in this work were from sources collected at low temperature (4–143 K) or otherwise corrected to reduce this problem (see Supporting Information). For comparison of the computed isomer shifts with the various functionals to high-temperature (298 K) data, one needs to subtract a temperature correction of approximately 0.06 ± 0.03 mm/s. Most relevant to the present work is the isomer shift of deoxyMb and deoxyHb varying from 0.92–0.93 mm/s at 4.2 K to 0.86 mm/s at 195 K, with most of the effect occurring after 100 K.¹⁰³

RESULTS AND DISCUSSION

Calibration of Mössbauer Isomer Shifts. The full results of the calibration between computed electron densities at the iron nucleus and experimental low-temperature δ values are provided in the Supporting Information. The mean absolute errors (MAEs) for the computed vs experimental δ values and the squared linear correlation coefficient of the regression curves are given in Table 1 for five functionals: TPSSh,^{53,54}

Table 1. Mean Absolute Errors (MAEs) and Correlation Coefficients (R^2) for Computed Isomer Shifts (mm/s) of Five Density Functionals^a

	TPSSh	BP86	B3LYP	PBE0	PBE
MAE	0.037	0.056	0.051	0.053	0.061
R^2	0.990	0.982	0.984	0.982	0.978

^aSee the Supporting Information for details.

BP86,^{55,56} B3LYP,^{47,51,104} PBE0, and PBE spanning 0–25% HF exchange and variations in design strategy. The results show that all functionals can provide accurate linear fitting of δ , similar to previous conclusions.⁸⁶ The correlation coefficients from 0.98 to 0.99 are similar to those reported before, whereas the mean average errors are slightly smaller than those for other data sets using similar procedures,^{84–88} possibly because the present calibration used Cosmo-optimized monoiron complexes. The order of performance was TPSSh > B3LYP > PBE0 ~ BP86 > PBE, i.e., hybrid functionals performed better than nonhybrids, and was consistent with an optimum of HF exchange smaller than 20%. The small MAE of TPSSh of ~0.04 mm/s could suggest that physical constraints on this functional, e.g., the independence of the exchange energy on the reduced gradient near the nucleus,⁵³ may improve its accuracy, although this requires more investigation. For iron(II) systems alone, correlation was slightly lower, 0.97 (see Supporting Information). For the relative changes in δ due to changes in electronic structure, any of these functionals is likely to provide reasonable results since systematic errors will tend to cancel during fitting when the same system is studied only under small perturbations.

Computation of Deoxyheme and Oxyheme Isomer Shifts.

The experimentally determined isomer shifts for globin hemes are shown in the last column of Table 2: δ is 0.27 mm/s for oxyheme (oxyHb, 77 K)^{105,106} and 0.92 vs 0.86 mm/s for deoxyheme at 4.2 K vs 195 K¹⁰³ (deoxyMb, similar for deoxyHb).^{96,107} δ for deoxyMb increases 0.03 mm/s from 83 to 4 K, suggesting that δ for oxyheme at 4.2 K can be estimated to be ~0.30 mm/s. δ values of various oxyheme compounds generally suggest a decrease of ~0.10 mm/s from low to high temperature.¹⁰⁸ For example, δ of the deoxy complex Fe(TPP)(2-MeIm) changes from 0.93 mm/s at 4.2 K to 0.82 mm/s at 300 K. δ values for a variety of synthesized imidazolydeoxyheme models fall in the range 0.85–0.95 mm/s.¹⁰⁹

The computed δ values of deoxyheme and oxyheme with His as distal ligand are 0.99 and 0.42 mm/s, respectively, using the Cosmo-optimized porphine models. This is 0.07 and 0.12 mm/s off the experimental values when correcting for temperature, which is in line with typical uncertainties from DFT computations^{84–86} but worse than the present work's optimal fit with MAE ~ 0.04 mm/s.

A substantial part of the difference between experimental and predicted isomer shifts could be due to the heme side chains affecting the electron density on iron. To test this, for a full heme model with side chains (Supporting Information, Figure S4), the computed isomer shift decreases from 0.99 to 0.93 mm/s for deoxyheme, implying that the heme side chains cause a withdrawing of electron density corresponding to 0.06 mm/s, which is substantially more than one would anticipate given the distance of the substituents from the iron center. The isomer shift decreases due to the removal of electron density from iron, i.e., the side chains act as electron-withdrawing groups, possibly further enhanced by hydrogen bonding in the full proteins. With this in mind, and correcting for temperature, the predicted isomer shift for deoxyheme is excellent (0.93 vs 0.92 mm/s), and assuming a similar electron-withdrawing effect in oxyheme, 0.42 mm/s reduces to 0.36 mm/s when correcting for side chains, in good agreement with the interpolated ~0.30 mm/s at low temperature for oxyheme and very similar to the 0.33 mm/s computed previously by Shaik and co-workers.¹³

Computed Structures of Deoxyheme and Oxyheme.

The optimized structures have been compared with the atomic resolution structures of deoxyMb and oxyMb in Table 2. Although the modest accuracy of protein crystallography near metal sites prevents a quantitative benchmark even for atomic-resolution protein structures,^{110–113} computed and crystal bond lengths and angles are still expected to be in reasonable agreement, i.e., within 0.05 Å at least. For metal–ligand bonds of diatomics, where dispersion and solvation effects are absent, various functionals, notably BP86, give small mean absolute errors of <0.03 Å,⁶¹ and on average such an accuracy is

Table 2. Comparison of Experimental and Computed Structures and Mössbauer Isomer Shifts^a

system	Fe–O (Å)	O–O (Å)	Fe–N _{ax} (Å)	Fe–N _{eq} (Å)	Fe–O–O (deg)	δ (mm/s)
deoxyMb (1A6N) ^b	–	–	2.15 ^b	2.05, 2.06, 2.07, 2.11	–	0.92 (4.2 K) ^c
deoxyheme, computed (porphine)	–	–	2.123	2.093, 2.095, 2.098, 2.100	–	0.99
deoxyheme, computed (full heme)	–	–	2.118	2.085, 2.091, 2.100, 2.112	–	0.93
oxyHb	–	–	–	–	–	0.27 (77 K), ^d ~0.30 (4.2 K)
oxyMb (1A6M) ^b	1.81	1.24	2.06	2.00, 2.00, 2.00, 2.02	123	–
oxy, computed (porphine)	1.84	1.29	2.04	2.004, 2.005, 2.027, 2.028	121	0.42

^aMb, myoglobin; Hb, hemoglobin. ^bReference 76. ^cReference 103. ^dReferences 105 and 106.

Table 3. Computed Structural Properties and Spin Densities of Singlet HemeO₂ Adducts: Fe–O Bond Lengths, O–O Bond Lengths, O··H Hydrogen Bond Lengths, Fe–O–O Angles, Fe–N_{ax} Bond Lengths to the Proximal Histidine (from BP86/Cosmo), and Spin Density (SD) on Fe, OA (Bound to Fe), and OB (Bound to OA) (from TPSSH/Cosmo)

system	Fe–O (Å)	O–O (Å)	O··H (Å)	Fe–O–O (deg)	Fe–N _{ax} (Å)	SD(Fe) (au)	SD(OA) (au)	SD(OB) (au)
Heme Models without Distal Water								
HisO ₂	1.838	1.288	1.883 (A)	121.3	2.036	1.02	−0.34	−0.62
HipO ₂	1.859	1.292	1.702 (A)	121.3	2.037	−1.04	0.33	0.64
GlnO ₂	1.829	1.289	2.016 (B)	121.4	2.050	−1.02	0.37	0.59
LysO ₂	1.863	1.296	1.688 (A)	122.3	2.029	−1.02	0.33	0.64
ArgO ₂	1.828	1.300	1.895 (B)	121.0	2.031	1.00	−0.41	−0.53
TrpO ₂	1.844	1.287	1.959 (A)	120.6	2.063	−1.03	0.35	0.62
AlaO ₂	1.832	1.281	0.000	120.5	2.081	−1.04	0.36	0.61
ValO ₂	1.832	1.280	0.000	120.6	2.084	−1.03	0.36	0.61
LeuO ₂	1.823	1.281	0.000	120.9	2.058	1.01	−0.35	−0.60
Heme Models with Additional Distal Water								
HisO ₂ H ₂ O	1.852	1.294	2.015	118.8	2.050	−1.03	0.37	0.60
HipO ₂ H ₂ O	1.839	1.302	1.726	121.0	2.023	−1.01	0.34	0.60
GlnO ₂ H ₂ O	1.828	1.288	1.850	120.0	2.065	−1.01	0.37	0.58
LysO ₂ H ₂ O	1.837	1.302	2.022	120.5	2.009	−1.00	0.37	0.59
ArgO ₂ H ₂ O	1.833	1.298	1.675	119.3	2.031	−1.00	0.38	0.56
TrpO ₂ H ₂ O	1.831	1.295	1.938	122.6	2.040	−1.00	0.39	0.56
AlaO ₂ H ₂ O	1.822	1.292	1.833	120.2	2.041	−1.00	0.37	0.58
ValO ₂ H ₂ O	1.818	1.292	1.817	120.6	2.040	−0.99	0.36	0.58
LeuO ₂ H ₂ O	1.821	1.289	1.904	120.3	2.049	1.01	−0.38	−0.56

expected, as also seen from Table 2. In contrast, B3LYP gives Fe–O bond lengths of ~ 1.88 – 1.89 Å,¹² consistent with the known tendency of this functional to produce too long and weak metal–ligand bonds.^{40,61} Still, since random errors in metal–ligand bonds from crystallography can exceed this, the maximum deviations can be slightly larger in some cases, notably for soft bonds.

For the deoxyheme, the Fe–N_{ax} distance between iron and the imidazole group of the proximal His is expected to be longer than in the oxyheme due to out-of-plane movement of iron; the crystal estimate is 2.15 Å.⁷⁶ This bond is 2.123 Å when computed with the Cosmo solvent model as done throughout this work, versus 2.136 Å for a vacuum optimization, showing that the solvent screening reduces the proximal bond length by 0.013 Å, which is significant. Including the full heme with side chains reduces this bond further by 0.005 Å, which is less significant.

For the equatorial distances, which are affected by the iron out-of-plane movement occurring in the deoxy state, agreement is also excellent. For deoxyheme, the average of the experimental Fe–N_{eq} bonds is 2.08 Å, vs 2.10 Å computed (2.097 Å). Including the heme side chains reduces the average by 0.002 Å, which is much less than the uncertainties in experimental and theoretical bond lengths. A vacuum optimization reduces the average from 2.097 to 2.094 Å; i.e., the condensed phase screening as used throughout this work marginally reduces the out-of-plane movement. While the heme side chains were shown to withdraw substantial electron density from the iron center affecting significantly the isomer shifts, the subtle geometry corrections of 0.002 and 0.003 Å suggest that the porphine model is accurate for describing the local geometry around iron.

For oxyheme, all computed bonds are within 0.03 Å of the crystal structures, except the O–O bond in the oxyheme, which is 0.05 Å shorter in the crystal structure. The crystal distance resembles neutral, free O₂ and mainly reflects the neutral O₂ parameters used for structure refinement. The O–O bond,

computed to be 1.29 Å, is expected to resemble superoxide (O–O ~ 1.33 Å), as discussed below for the vibrations. The Fe–O–O angle is quite similar (deviates by 2°) in the crystal and DFT structures.

For oxyheme, the Fe–N_{eq} distances fall into two pairs separated by roughly 0.02 Å. This can be explained as being due to the splitting of the e-level when breaking the C_{4v} symmetry as the bent O₂ and imidazole π -systems interact differently with the porphyrin ring along the x - and y -axes. The two molecular orbitals dominated by atomic orbitals d_{xz} and d_{yz} are then singly and doubly occupied, thus producing two minima for iron's relative position along the x - and y -axes. As the electrostatic repulsion between the imidazole π -system and the d-electrons is reduced by condensed phase screening, the Cosmo-optimized heme model has slightly less symmetry breaking.

Effect of Distal Interactions on Electronic Structure of HemeO₂. After validating the oxy- and deoxyheme models against experimental data, we now turn to the focus of this work, which is to understand systematically the impact of distal hydrogen bonds on the electronic structure and spectroscopic properties of hemeO₂. Table 3 shows optimized bond distances, the Fe–O–O angle, and spin densities of the FeO₂ moiety for a range of heme models where O₂ interacts with distal groups resembling combinations of water and side chains of position E7.

The distal hydrogen bond in the HisO₂ model was found from early BP86 calculations to compress the Fe–O bond by ~ 0.01 Å (from 1.81 to 1.80 Å) and elongate the O–O bond by ~ 0.02 Å (from 1.29 to 1.31 Å).¹⁷ The anticorrelation between the bonds is expected from the back-bonding of Fe d _{π} into O–O π^* , which increases with stronger Fe–O bonding.^{25,114} By performing vacuum optimizations with BP86, we obtained Fe–O = 1.808 Å and O–O = 1.284 Å. In more realistic Cosmo optimizations, electrostatic screening will change the distal effects and the bond lengths change substantially to 1.838 and 1.288 Å, respectively, showing a surprisingly large solvent effect on the Fe–O bond of +0.03 Å. A simple explanation for this

solvent effect is that the distal interaction is screened, thus reducing the strength of the partly ($\sim 50\%$) ionic¹¹⁵ Fe–O bond.

In our calculations, the Fe–O bond elongates by ~ 0.01 Å due to His relative to the average of the three models with hydrophobic side chains (AlaO₂, ValO₂, and LeuO₂), showing that the Fe–O bond length does not anticorrelate with K_{O_2} as might otherwise be expected. The O–O bond length increases by 0.01–0.02 Å (from ~ 1.28 to ~ 1.29 – 1.30 Å) due to distal hydrogen bonds, mostly with the long cationic side chains Lys and Arg. This increase is consistent with increased back-donation into O₂ despite the longer Fe–O bond, which would in itself reduce back-donation. The bond lengths of O₂ and O₂[−] are ~ 1.21 and 1.33 Å. Assuming a linear relation between superoxide character and O–O bond length, the distal hydrogen bond changes the heme O–O bond from being $\sim 58\%$ to $\sim 75\%$ superoxide character when elongating from 1.28 to 1.30 Å. Thus, distal hydrogen bonding in heme proteins stabilizes the overall FeO₂ moiety, elongates both Fe–O and O–O bonds, and leads to a net increase in back-donation, probably because the proton partial charge draws more electron density into π^* than is lost by the $+0.01$ Å Fe–O bond length. This counterintuitive effect in the presence of distal interactions may be universally relevant to metal-to-ligand back-bonding leading to ligand-activation during catalysis, e.g., in iron oxygenases.

The O...H bond lengths are shown in the fourth column of Table 3. It is important to notice that some of the side chains, due to their steric preferences, tend to prefer either oxygen A or oxygen B (where OA is bound to iron). This difference is important as the two types of hydrogen bonds can be seen to have different effects on the electronic structure, as witnessed from the spin densities on OA and OB: The OA hydrogen bonds on average have 0.63 spin on OA and 0.34 on OB, whereas the OB hydrogen bonds on average change spin densities to 0.56 and 0.39 for OA and OB (the absence of hydrogen bonds gives values in between these two cases). In the wild type (WT), both forms can exist, and we have thus investigated both alternatives and how they are affected by a distal water (vide infra). OA hydrogen bonds generally tend to give ~ 0.01 – 0.04 Å longer Fe–O bonds compared to both hemes with OB hydrogen bonds and hemes without any hydrogen bonds, but the hydrogen bond type has a minor influence on the O–O bond length. The stronger hydrogen bonds to OA in LysO₂ and HipO₂ give the longest Fe–O bonds, which can be explained again by the ionic model of Fe–O₂ bonding, reducing the bond strength when the O₂ partial negative charge is reduced by the hydrogen bond.

The Fe–O–O angle may be an important structural property of hemeO₂ adducts.¹¹⁶ The bent $\sim 120^\circ$ angle for hemeO₂ vs the nearly linear Fe–C–O angle for hemeCO shows that, in the globins, the hybridization expected from the free ligands prevails in the bound complexes. Thus, the Fe–O–O and Fe–C–O angles indirectly testify to a modest electronic reorganization during binding, consistent with the reversible binding in the globins. The main conclusion from the computed Fe–O–O angles in Table 3 is that distal hydrogen bonding increases the angle by $\sim 1^\circ$, although the specifics of the conformation of each type of interaction will affect the angle, too, as seen for the long, sterically demanding Lys group. The effects are small and not very systematic; i.e., overall, the

Fe–O–O angle is a relatively poor proxy of the electronic structure of hemeO₂ adducts, to be elaborated below.

The last geometric property discussed here is the Fe–N_{ax} distance to the proximal histidine (modeled as imidazole). It decreases from 2.06–2.08 to 2.03–2.05 due to hydrogen bonding, i.e., changes of a similar magnitude as the 0.01–0.04 Å elongation in Fe–O observed with different types of distal hydrogen bonds. The simple explanation for this tendency is the trans influence of the O₂ group; i.e., strong hydrogen bonding elongates Fe–O as explained, thus reducing the trans influence, allowing the proximal imidazole to approach more closely.

The second part of Table 3 shows the effect of including a water molecule on the distal side together with the E7 side chain group. The Fe–O bonds of the hydrophobic models AlaO₂, ValO₂, and LeuO₂ change insignificantly upon adding water hydrogen bonding to O₂, but the hydrogen bond from water is still strong enough to reduce the trans influence of O₂, leading to a compression of the Fe–N_{ax} bonds by 0.01–0.04 Å, i.e., slightly less than for the amino acid hydrogen bonds. In contrast, the systems where hydrogen bonds were already present have their Fe–O bonds modulated substantially in a nontrivial way by the competition between several hydrogen donors, and the effect of the water hydrogen bond on Fe–N_{ax} is smaller in these cases because they already had a reduced trans influence due to their amino acid hydrogen bonds. More systematically, the Fe–O–O angle is generally reduced, sometimes below 120° , by the presence of several hydrogen bond donors. Also of interest is the observation that the spin densities for the water models tend to have 0.37 ± 0.02 and 0.58 ± 0.02 spin on OA and OB; i.e., the tendency of OA hydrogen bonds to spin polarize the O₂ moiety is reduced by the presence of additional hydrogen bonds.

Effect of Distal Interactions on Vibration Frequencies of HemeO₂. After having discussed the effects of distal hydrogen bonds on the electronic structure of hemeO₂, we turn to a discussion of how this manifests in spectroscopic properties. Table 4 shows the computed Fe–O, O–O, and Fe–porphine vibrations and the computed Mössbauer isomer shifts for the same 18 models as in Table 3.

For comparison, the Fe–O vibration of unprotected oxyheme produced from hemins was estimated at 573–574 cm^{−1}, with a characteristic iron–porphyrin band occurring also at 396 cm^{−1},¹¹⁷ consistent with picket-fence [Fe(TpivPP)(1-methylimidazolyl)O₂] showing an Fe–O band at 571 cm^{−1} and two bands near 400 cm^{−1}.²³ The O–O stretch $\nu(\text{O–O})$ has been estimated at 1159 cm^{−1} from picket-fence [Fe(TpivPP)(1-methylimidazolyl)O₂]¹¹⁸ and 1103 cm^{−1} for oxyMb,¹¹⁹ very similar to free superoxide (1100–1150 cm^{−1}).¹¹⁸ Both $\nu(\text{O–O})$ and the O–O bond lengths discussed above imply that O–O has a bond order of $\sim 1\frac{1}{2}$, which is fulfilled by, e.g., a Weiss¹²⁰ ²Fe(III)–²O₂ representation of oxyheme, but could also result from a mixture of configurations such as Pauling,^{121,122} McClure,¹²³ or Goddard-Olafson^{124,125} if approximately one net π^* electron is added to O–O without transferring a full electron to the actual O₂ moiety, i.e., if back-donation is compensated by donation of electron density away from O₂ in the Fe–O σ -bond¹³ or via the lone pairs along the distal hydrogen bonds.

Our computed $\nu(\text{Fe–O})$ of 548 cm^{−1} is 25 cm^{−1} off the estimated value from unprotected hemeO₂, which is reasonable, and a better accuracy cannot be expected. It provides an accurate starting point for estimating the effect of distal

Table 4. Computed Fe–O, O–O, and Fe–Porphine Vibration Frequencies (from BP86/Cosmo), and Isomer Shifts (TPSSH/Cosmo) for Singlet HemeO₂ Adducts

system	$\nu(\text{Fe–O})$ (cm ^{−1})	$\nu(\text{O–O})$ (cm ^{−1})	$\nu(\text{Fe–Por})$ (cm ^{−1})	δ (mm/s)
unprotected oxyheme ^a	571–574	–	396	–
picket-fence oxyporphyrin ^b	560–570	1159	–	–
MbO ₂ ^c	572	1103	–	–
Heme Models without Distal Water				
HisO ₂	548	1221	381, 398, 418	0.42
HipO ₂	452	1223	400	0.42
GlnO ₂	548	1232	379, 397, 420	0.42
LysO ₂	556	1185	373, 397, 426	0.42
ArgO ₂	465	1149	393	0.39
TrpO ₂	530	1236	375, 398, 412	0.44
AlaO ₂	532	1272	374, 397, 412	0.44
ValO ₂	531	1271	373, 396, 412	0.44
LeuO ₂	540	1270	376, 397, 414	0.43
Heme Models with Additional Distal Water				
HisO ₂ H ₂ O	533	1214	377, 399, 414	0.42
HipO ₂ H ₂ O	545	1173	375, 402, 414	0.39
GlnO ₂ H ₂ O	542	1235	379, 397, 417	0.42
LysO ₂ H ₂ O	547	1163	381, 397, 417	0.39
ArgO ₂ H ₂ O	516	1183	383, 413	0.40
TrpO ₂ H ₂ O	538	1202	378, 397, 414	0.41
AlaO ₂ H ₂ O	461	1243	393, 397	0.40
ValO ₂ H ₂ O	551	1224	380, 398, 423	0.40
LeuO ₂ H ₂ O	540	1234	376, 396, 414	0.41

^aReferences 23, 33, and 117. ^bReference 118. ^cReference 33 and references therein.

perturbations on the vibration of the Fe–O bond, in the context of the previous discussions. Notably, the effect of the protein's distal E7 is seen in the ~ 16 cm^{−1} increase in $\nu(\text{Fe–O})$ going from Ala (532 cm^{−1}) to His (548 cm^{−1}), comparing well to the tendency of lower vibrations of 6-coordinate methylimidazolyl picket-fence hemes (~ 560 cm^{−1}) relative to proteins (~ 570 cm^{−1}).³⁵

In contrast, $\nu(\text{O–O})$ is computed to be ~ 1221 cm^{−1}, which is ~ 100 cm^{−1} larger than experimental estimates. However, several components are known to contribute to the spectrum in this region with some components being of the order of 1150 cm^{−1}. Still, the error is larger, reflecting also the larger numerical value of the frequency. In addition to the theoretical uncertainty, it is plausible that the local solvent and protein interactions can affect the experimental values. This is supported by our calculations of vibrations with variable distal hydrogen bonds, including water, showing that in the presence of more or strong hydrogen bonds, $\nu(\text{O–O})$ will move considerably down.

Some Fe–O stretch vibrations are, like the O–O stretch, clean, whereas others are mixed. Notably, protonated histidine and arginine give almost-clean Fe–O vibrations at lower wavenumbers, 452 and 465 cm^{−1}, respectively, compared to His (548 cm^{−1}). At the same time, the O–O stretch frequencies of systems with hydrogen bonds are generally smaller than without, in particular for Arg (1149 cm^{−1}). This shows that hydrogen bonding enables more electron density to reside in the π^* orbitals of O₂, and that hydrogen bonding or partial proton transfer thus weakens the O–O bond of iron-bound O₂; this could be relevant for enzymes where the O–O bond needs

to be activated. In the globins, the hydrogen bond weakens the O–O bond but at the same time strengthens the Fe–O bond, due to the anticorrelation between Fe–O and O–O, leading to increased bond strength and thus oxygen affinity. The hydrogen-bonded Fe–O stretch frequencies at ~ 550 cm^{−1} are also strongly coupled to the motion of the hydrogen, but are otherwise clean. The commonly observed vibrations, typically two to three at 370–420 cm^{−1}, involve iron, oxygen, nitrogen, and carbon atoms of the porphyrin ring.

The trends in vibrations, e.g., the increase in $\nu(\text{O–O})$ for hydrophobic interactions and the reduction in both $\nu(\text{O–O})$ and $\nu(\text{Fe–O})$ for the strongly perturbing Arg side chain, may be useful in understanding distal interactions with FeO₂ directly from vibrations relative to a reference, e.g., a wild-type protein. For example, for Arg, one would predict 20–70 cm^{−1} smaller frequencies, which should be visible in a Raman spectrum. As an example, there is generally little knowledge about the variation in mammalian hemoprotein genes, but human hemoglobin variants are widely explored, and some observed variants include E7 mutations, e.g., the Zürich β -Hb variant (H64R)¹²⁶ and the Boghé α -Hb variant (H64Q).¹²⁷ Using spectroscopic fingerprints such as the change in $\nu(\text{O–O})$ might be useful for rapid identification of such E7 variants, but the regularities may also be relevant to other heme proteins with other interactions as the general effect of electron withdrawal from hydrogen bond donors should be relevant also in such cases.

Impact of Hydrogen Bonds on Mössbauer Isomer Shifts. Table 4 also shows the computed Mössbauer isomer shifts of the oxygen adducts, and Table 5 shows the computed

Table 5. Computed Spin Densities on Iron and Isomer Shifts of Deoxy Heme Models (Using TPSSH/Cosmo)

system	SD(Fe) (au)	δ (mm/s)
deoxyHis	3.77	0.99
deoxyHip	3.82	0.93
deoxyGln	3.85	0.93
deoxyLys	3.75	0.98
deoxyArg	3.84	0.93
deoxyTrp	3.85	0.92
deoxyAla	3.77	0.99
deoxyVal	3.78	0.99
deoxyLeu	3.77	0.99

isomer shifts and spin densities on iron for deoxy states with variable distal interactions. For the oxyhemes, the isomer shifts fall in the range from 0.39 to 0.44 mm/s (remember that, to estimate absolute experimental values, these should be corrected for the heme side chain effect of -0.06 mm/s). The hydrophobic interactions tend to have the highest isomer shifts, consistent with their poor electron-withdrawing capability, whereas the hydrogen bond donor interactions can withdraw electron density from iron, giving isomer shifts 0.05 mm/s lower, as seen for the Arg interaction, which has several hydrogen donor sites and a long side chain suitable for optimal contact and electron withdrawal. When additional hydrogen bond donors are added from water (bottom part of Table 4), δ is further reduced in most cases, with five systems reaching the 0.39–0.40 mm/s.

In addition to heme side chains that withdraw electron density from iron resulting in a 0.06 mm/s reduction in δ , distal electron-deficient groups can further reduce the isomer shift by

Table 6. Correlation Coefficients for Properties of All 18 HemeO₂ with Variable Distal Interactions^a

	Fe–O (Å)	O–O (Å)	Fe–O–O (deg)	$\nu(\text{Fe–O})$ (cm ^{−1})	$\nu(\text{O–O})$ (cm ^{−1})	δ (mm/s)	SD(Fe) (au)	SD(OA) (au)	E(Fe–O) (kJ/mol)
Fe–O (Å)	1	+0.245	+0.176	−0.063	−0.277	+0.243	−0.560	−0.609	+0.206
O–O (Å)	−	1	+0.045	−0.145	−0.952	−0.856	+0.554	+0.195	+0.440
Fe–O–O (deg)	−	−	1	+0.104	−0.130	+0.014	−0.032	−0.225	+0.413
$\nu(\text{Fe–O})$ (cm ^{−1})	−	−	−	1	+0.089	+0.180	+0.074	−0.175	−0.220
$\nu(\text{O–O})$ (cm ^{−1})	−	−	−	−	1	+0.773	−0.498	−0.234	+0.342
δ (mm/s)	−	−	−	−	−	1	−0.813	−0.386	+0.520
SD(Fe) (au)	−	−	−	−	−	−	1	+0.533	−0.545
SD(OA) (au)	−	−	−	−	−	−	−	1	−0.196
E(Fe–O) (kJ/mol)	−	−	−	−	−	−	−	−	1

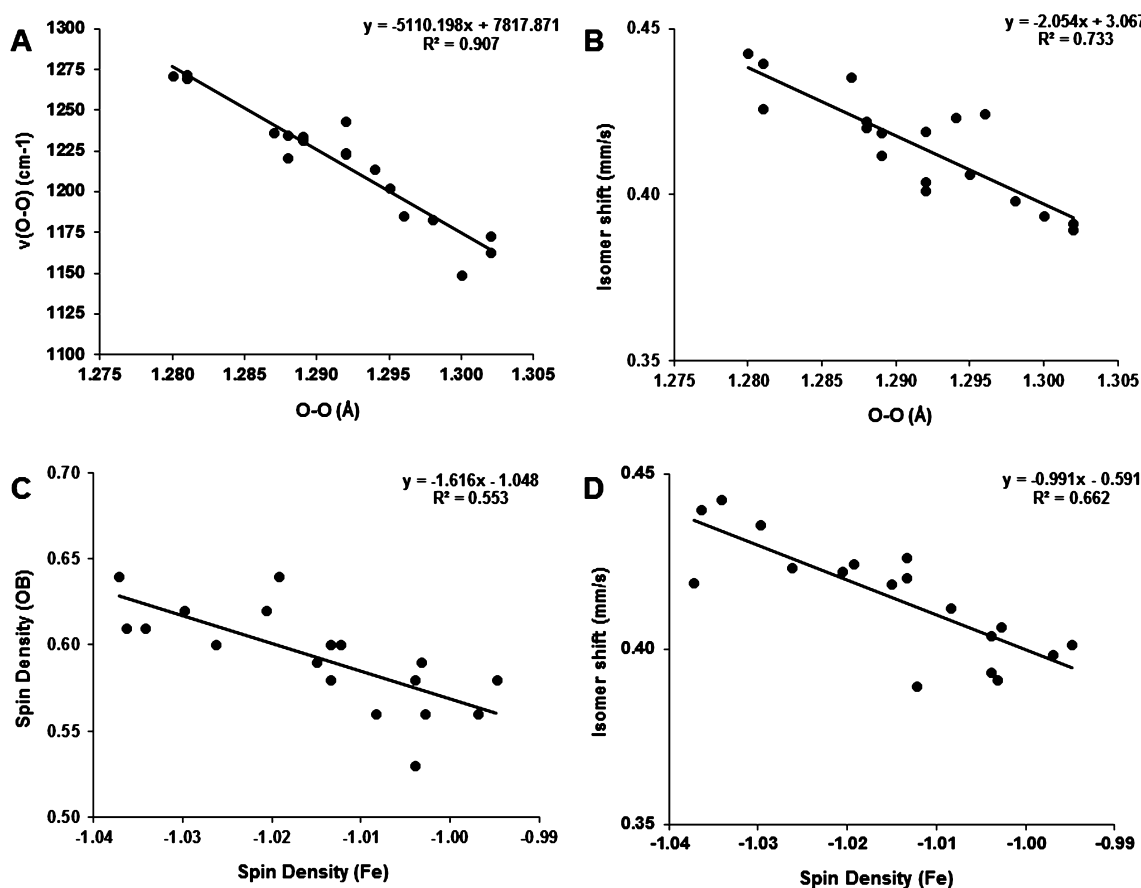
^aValues larger than 0.5 are shown in italics.

Figure 2. Notable correlations between properties of oxyheme models studied in this work. In (A) and (B), stronger hydrogen bonding is associated with the lower right points, more back-donation, weaker O–O bonds, and smaller isomer shifts due to reduced electron density on iron. (C) Spin polarization is a persistent phenomenon across the hemes with high correlation; strongly hydrogen bonded systems tend to be more polarized, viz., top left of (C), corresponding to the Weiss picture. (D) The correlation between isomer shifts and spin densities of iron is significant.

up to 0.07 mm/s, as seen in some deoxy states in Table 5, consistent with the data from Table 4. The three hydrophobic interactions give $\delta \sim 0.99$ mm/s (similar to His), whereas other, positively charged or longer hydrogen-bond donors can reduce δ to 0.92 mm/s. This analysis may potentially help in deducing a heme environment from accurately measured Mössbauer spectra versus a reference heme. Using the example above of hemoglobin variants, the Zürich variant H64R would be predicted to exhibit a ~ 0.03 mm/s smaller isomer shift than the wild type for the oxy adduct, and potentially 0.06 mm/s smaller for the deoxy state.

Correlations between Structural and Spectroscopic Data. To investigate further the relation between spectroscopic

properties as proxies of structural changes in heme systems, several properties have been correlated against each other for the hemeO₂ systems, as shown in Table 6 (the corresponding data only for the nonhydrated systems can be found in the Supporting Information, Table S7). Correlation coefficients (r) numerically larger than 0.5 are in italics.

Starting with the Fe–O bond, several significant correlations can be seen across all the systems. Most surprising is perhaps the poor correlation ($r \sim -0.063$) between $\nu(\text{Fe–O})$ and the Fe–O bond length, which would, *ceteris paribus*, be anticorrelated. The absence of correlation relates to the previous discussion on the diversity of hydrogen bond donor interactions and the coupling of several vibration modes, as

Table 7. Electronic Energies and Free Energies (kJ/mol) of Binding O₂ to Heme Models (kJ/mol) Using TPSSh or B3LYP with or without Dispersion with Cosmo, $\epsilon = 10$ or $\epsilon = 4$

system	B3LYP, $\epsilon = 10$	B3LYP-D3, $\epsilon = 10$	TPSSh, $\epsilon = 4$	TPSSh, $\epsilon = 10$	TPSSh-D3, $\epsilon = 10$	TPSSh-D3, $\epsilon = 10$ + scalar rel
Electronic Energies						
His	−44.0	−73.5	−100.7	−103.7	−128.7	−140.4
Hip	−32.3	−46.2	−83.8	−87.4	−99.7	−110.1
Gln	−32.0	−46.4	−86.1	−88.9	−100.4	−110.5
Lys	−39.7	−56.5	−90.7	−94.1	−108.5	−120.3
Arg	−40.5	−57.8	−96.0	−96.8	−111.2	−122.0
Trp	−28.9	−59.0	−81.4	−84.7	−110.4	−120.2
Ala	−27.7	−51.4	−83.0	−87.1	−107.3	−118.4
Val	−26.0	−50.9	−82.3	−85.7	−106.8	−117.9
Leu	−35.7	−52.9	−90.3	−94.8	−108.7	−120.2
av	−34.1	−55.0	−88.3	−91.5	−109.1	−120.0
Free Energies						
His	14.5	−15.0	−42.1	−45.2	−70.2	−81.9
Hip	36.0	22.1	−15.5	−19.1	−31.4	−41.8
Gln	35.5	21.2	−18.5	−21.3	−32.8	−43.0
Lys	38.0	21.2	−12.9	−16.3	−30.8	−42.5
Arg	31.4	14.0	−24.2	−25.0	−39.4	−50.1
Trp	40.7	10.7	−11.7	−15.0	−40.7	−50.5
Ala	53.9	30.2	−1.4	−5.5	−25.7	−36.8
Val	51.4	26.6	−4.9	−8.3	−29.3	−40.4
Leu	23.7	6.5	−30.9	−35.4	−49.3	−60.8
av	36.1	15.3	−18.0	−21.2	−38.8	−49.8

they can both work to a correlation and anticorrelation between the bonds: Elongation of both Fe–O and O–O is as mentioned seen upon hydrogen bonding despite associated higher O₂ affinity (experimentally and discussed below), which can be explained using the ionic binding model. Thus, despite the elongation of Fe–O due to the pull of the distal hydrogen bonds, back-donation is enhanced by the electron withdrawal toward the hydrogen bond, elongating the O–O bond while—perhaps counterintuitively—strengthening the more ionic Fe–O bond despite this elongation.

Thus, in distal hydrogen-bonded systems (which will commonly be observed in proteins and proton-donor solvents), Fe–O is instead weakly correlated with O–O and $\nu(\text{O–O})$ but correlated with the spin densities of iron and oxygen ($r \sim -0.56$ – 0.61 , $r^2 \sim 0.66$, see Figure 2D). The significant anticorrelation between spin density and Fe–O bond length can be understood as arising from the Weiss configuration, which makes up roughly half¹⁵ of the hemeO₂ ground state. Spin polarization, evident from Figure 2C, is a proxy of the contribution of this Fe(III)–O₂[−] configuration, which increases with distal hydrogen bonding due to the electron-withdrawal ionic-bonding mechanism described above. As electron density is favored in the O₂ ligand by hydrogen bonding, and Fe–O is elongated, the Weiss configuration increases in weight, which in DFT is represented by increased spin polarization.

The strongest among all identified correlations is, perhaps not surprising, between the O–O bond length and stretch frequency. The correlation coefficient is -0.95 ($r^2 \sim 0.907$) for the 18 hemeO₂ systems studied (Figure 2A) and -0.98 when considering only the models without water (Table S7 in the Supporting Information). This strong correlation is related to the clean (i.e., weakly coupled) O–O stretch, which is thus behaving differently from the Fe–O bond. Thus, in all cases of studied heme systems, whereas the $\nu(\text{Fe–O})$ stretch frequency is a poor proxy of the structure of the FeO₂ moiety, $\nu(\text{O–O})$ is a robust proxy of the O–O bond length. Also, as seen in Figure

2B, the isomer shift is interestingly anticorrelated with the O–O bond length ($r \sim -0.86$, $r^2 \sim 0.73$) and, hence, positively correlated with $\nu(\text{O–O})$ ($r \sim +0.77$). Again the ionic model of bonding is the best framework for rationalizing the change in isomer shift: Hydrogen bonding leads to both increased ionic bonding (in wave function language, increased contribution of the Weiss configuration) and stronger back-donation, giving a weaker and longer O–O bond. These results are thus fully consistent with previous observations that the protein increases the Weiss character of the adduct.¹³ The transfer of electron density from iron to the O₂ π^* orbitals simultaneously leads to a quite systematic reduction in isomer shift, explaining why isomer shift and $\nu(\text{O–O})$ are so substantially correlated.

The computed energy of O₂ binding has also been correlated against other properties (the energetics will be discussed separately below). While the absolute energy depends dramatically on the choice of functional and corrections, the correlation is robust as the relative energies of the systems are fairly constant (vide infra). Most interesting is the observation that the spin density of iron, the isomer shift, and the binding energy are all correlated with $|r| > 0.5$. As the isomer shift decreases from 0.44 to 0.39 mm/s, with high significance, the bound complex is stabilized across a range of ~ 50 kJ/mol. Our rationale for this observation is that, as the Weiss configuration increases with hydrogen bonding, the isomer shift is reduced while the spin density increases, and the hydrogen bonding at the same time leads to an increase in the binding energy due to stabilization of the bound O₂. This suggests that, for closely related heme proteins (e.g., mutants vs wild type), the species with the lower isomer shift is likely to indicate a higher O₂ affinity (i.e., lower P_{50}).

Thermodynamics of O₂ Binding. After having discussed key relations between spectroscopic properties and electronic structure as a function of distal hydrogen bond type, we now discuss the computation of oxygen binding thermodynamics for the various models. As a basis for discussion, the numbers have

Table 8. Electronic Energies and Free Energies (kJ/mol) of Binding O₂ to Hydrated Heme Models (kJ/mol) Using TPSSh or B3LYP with or without Dispersion with Cosmo, $\epsilon = 10$ or $\epsilon = 4$

system	B3LYP, $\epsilon = 10$	B3LYP-D3, $\epsilon = 10$	TPSSh, $\epsilon = 4$	TPSSh, $\epsilon = 10$	TPSSh-D3, $\epsilon = 10$	TPSSh-D3, $\epsilon = 10$ + scalar rel
Electronic Energies						
His	−43.9	−80.7	−96.5	−102.6	−133.9	−145.6
Hip	−34.3	−67.0	−87.7	−91.0	−119.6	−130.6
Gln	−35.8	−59.7	−90.6	−96.0	−115.9	−126.0
Lys	−61.5	−87.2	−119.1	−121.0	−143.2	−155.6
Arg	−41.0	−67.5	−101.2	−101.3	−123.9	−134.6
Trp	−27.6	−68.3	−79.3	−85.1	−119.3	−129.7
Ala	−36.4	−71.3	−90.9	−97.9	−127.6	−139.6
Val	−37.5	−77.2	−92.4	−98.6	−132.1	−144.2
Leu	−36.3	−70.4	−88.6	−96.6	−124.9	−136.8
av	−39.4	−72.1	−94.0	−98.9	−126.7	−138.1
Free Energies						
His	47.4	10.6	−5.2	−11.3	−42.7	−54.4
Hip	87.4	54.8	34.1	30.7	2.1	−8.9
Gln	79.0	55.0	24.2	18.7	−1.2	−11.3
Lys	55.2	29.4	−2.5	−4.4	−26.6	−39.0
Arg	87.3	60.8	27.1	27.0	4.4	−6.3
Trp	79.8	39.1	28.1	22.4	−11.9	−22.3
Ala	100.3	65.4	45.8	38.8	9.1	−2.9
Val	72.7	33.0	17.8	11.6	−21.9	−34.0
Leu	61.8	27.6	9.5	1.5	−26.9	−38.7
av	74.5	41.7	19.9	15.0	−12.8	−24.2

been compared to thermodynamic and kinetic data of O₂ binding for both wild-type sperm whale myoglobin and relevant mutants based on work by Olson and co-workers.^{31,128} The models are not accurate enough to capture the absolute energetics of O₂ binding, since additional distal effects, heme side chains, proximal effects, and long-range electrostatics will contribute. However, the relative changes in oxygen binding properties seen for the mutants of myoglobin should reflect the computed data as any shift due to the protein environment, etc. would cancel, *ceteris paribus*.

Tables 7 and 8 show the computed electronic energies (top of each table) and free energies (bottom of each table) corrected for zero-point vibrational energy, thermal effects, and entropy. In each case, numbers are provided for both B3LYP and TPSSh with and without D3 dispersion correction, and for TPSSh additionally with $\epsilon = 4$ or 10 and with scalar-relativistic corrections included. Given the accuracy of TPSSh from previous studies of ligand binding and spin cross-over,^{36,37,40,41,49} the last columns in the lower halves of Tables 7 and 8 are our preferred estimates of the relative free energies of O₂ binding for the nonhydrated and hydrated heme models, respectively. To these energies, corrections for the specific heme protein should be added to obtain absolute energies.

Starting with the top of Table 7, it can be seen that the computations correctly give the strongest O₂ binding with histidine (−44 kJ/mol energy for B3LYP, −104 kJ/mol with TPSSh) compared to an average binding energy of −34 kJ/mol for B3LYP and −95 kJ/mol for TPSSh. Thus, TPSSh gives ∼60 kJ/mol stronger binding than B3LYP, largely due to the 10% difference in HF exchange, being the single most important source of potential computational error in the study of metal–ligand binding.⁴⁹ This is consistent with the trend seen for BP86 (0% HF exchange) giving up to ∼100 kJ/mol stronger binding than B3LYP in other studies.²⁰ Correction for dispersion gives stronger binding, also fully consistent with previous results,²² and the rationale that tighter binding is

favored by attractive dispersion.^{37,49} The similar dispersion correction with both functionals is encouraging as it should be a real component of the total energy. For the nonhydrated water systems, it varies from 12 to 26 kJ/mol and for hydrated systems it varies from 20 to 34 kJ/mol, thus affecting also the relative O₂-binding energies by up to 14 kJ/mol, which is reasonable.

The value of ϵ is less important, with a change of <5 kJ/mol in O₂-binding energy. This is consistent with the overall charge neutrality of the process. As the Weiss picture of hemeO₂ contributes significantly as discussed above, it polarizes O₂, causing a higher dielectric constant to enhance binding as it screens the back-donated negative charge on O₂. Comparison of the last two columns of Table 7 shows that a scalar-relativistic correction favors O₂ binding by 10–12 kJ/mol across all systems (both hydrated and nonhydrated); i.e., for relative binding energies, it is not important.

Turning to the computed free energies, these numbers are for full ligand dissociation and are thus not directly comparable to the experimental data. The entropy corrections range from 58 to 82 kJ/mol at 298 K and favor dissociation for two reasons: The change to high spin in itself contributes roughly ∼25 kJ/mol of entropy favoring the dissociated state,⁴⁹ whereas ligand dissociation (gain of rotational and translational entropy) contributes the remainder. The latter estimate is too large due to the protein-dependent binding O₂ to secondary sites observed as the experimental “deoxy state”, reducing both the activation entropy and enthalpy of dissociation and the equilibrium state functions for full O₂ release.

An improved estimate is to use the hydration free energy of O₂. Whereas the enthalpy of hydration of O₂ is negligible due to its weak interactions with water (∼−1 kJ/mol),¹²⁹ $T\Delta S_{\text{hyd}}$ is of the order of ∼−15 kJ/mol as for other small neutral molecules at 298 K.^{130,131} For the relative free energies between the systems, this contribution cancels, but the correction is important when computing the absolute free energy. It cancels

approximately with the overestimation of the dispersion free energy correction to keep the free energies in the range of the numbers computed in the last column of Table 7, with -82 kJ/mol computed for His. The hydrogen bond energy for the WT has been estimated from previous calculations to be 32 kJ/mol, with an unknown compensating entropy effect.¹⁷ The experimental stabilization, as seen from Table 8, amounts to 10 – 15 kJ/mol, depending on whether K_{O_2} or dissociation barriers are used for estimating the free energy. Including dispersion, the difference from His to the hydrophobic groups is ~ 20 kJ/mol from Table 7, top, which is more reasonable in comparison to the experimental range considering a partial entropy compensation.

We now turn to the hydrated models in Table 8. The hydrated oxy states can be considered as probes of further hydrogen bond saturation to investigate how this modulates the distal E7 interaction. In metmyoglobin, water may in some deoxy states bind in the distal site, notably in the more polar mutants and in the WT,⁷⁸ so investigating the role of water as a distal interaction is relevant. Again, entropies are too large compared to any real protein due to the neglect of entropy loss associated with binding water and O_2 to secondary sites, and thus, only the relative numbers are of significance. On average, the water allows O_2 to bind ~ 18 kJ/mol more strongly to the heme. The general trends of B3LYP vs TPSSh, dispersion, Cosmo dielectric constant, and relativistic corrections apply consistently also to the hydrated systems. The stronger binding with additional saturation of hydrogen bonds importantly correlates with a number of properties as described above, which provides a good understanding of how a more saturated hydrogen bond network increases O_2 binding while activating more the O–O bond, favoring the Weiss configuration with the associated trends in isomer shifts and vibration frequencies of likely relevance also to nonheme FeO₂ systems.

Free Energies of O_2 Binding. Table 9 shows some experimentally determined free energies of O_2 binding and dissociation, compared with the computed free energies of O_2 binding. The dissociation of O_2 is rate-limiting relative to the association of water, but if present in the deoxy state, H_2O may still affect the association barriers and the relative K_{O_2} of

Table 9. Experimental Oxygenation Constants (K_{O_2}) and O_2 Dissociation Rate Constants (k_{-1}), Converted into Free Energies ($\Delta\Delta G$ and ΔG^*), and Computed Free Energies of O_2 Dissociation (ΔG) for Oxyheme with Various Distal Residues

system	exptl K_{O_2} ^a (μM^{-1})	$\Delta\Delta G$ ^b (kJ/mol)	exptl k_{-1} (s^{-1})	ΔG^* (kJ/mol)	calcd ΔG^c (kJ/mol)
His	1.1 ± 0.2	—	15	65	82
Hip	—	—	—	—	42
Gln	0.18	−4	130	60	43
Lys	—	—	—	—	43
Arg	0.09	−6	880	55	50
Trp	0.07	−7	87	61	51
Ala	0.02	−10	2300	53	37
Val	0.01	−11	10 000	49	40
Leu	0.02	−10	4100	51	61

^aReference 31. ^bFree energy of O_2 binding relative to wild type, $\Delta\Delta G_{O_2} = -RT \ln(K_{O_2}/K_{O_2}(WT))$. ^cFree energies of O_2 binding from Table 7, last column (TPSSh fully corrected).

mutants by favoring H_2O in polar, hydrophilic deoxy states, notably the WT (the WT dissociation rate of H_2O is ~ 10 times smaller than for other mutants, corresponding to roughly 5 kJ/mol).⁷⁸ Metmyoglobin is, due to the net charge near the ferric iron, more hydrophilic than ferrous myoglobin and thus overestimates water occupancies. Water is absent in hydrophobic mutants (e.g., H64V and H64L) but most likely present (with uncertain occupancy) in the more polar systems, notably the WT.⁷⁸ For this reason, our computed O_2 -binding free energies are most consistently compared to the dissociation barriers ΔG^* in Table 9.

At 293 K where thermokinetic data were measured, the WT sperm whale Mb dissociation rate constant corresponds to an effective activation free energy of ~ 65 kJ/mol. This barrier importantly includes entropy contributions, which favor dissociation, and specific protein and heme effects.^{132,133} The computed relative free energies of binding O_2 are in reasonable agreement with experimental data, as shown in Figure 3, with a

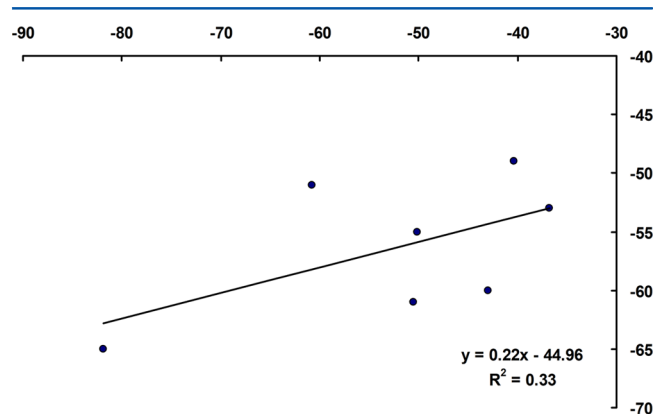


Figure 3. Correlation between computed O_2 -binding free energies and experimental dissociation barriers of oxyhemes of myoglobin mutants with variable distal interactions.

squared correlation coefficient of 0.33 and mean absolute deviation of ~ 4 kJ/mol (maximum deviation 10 kJ/mol). The unfitted computed numbers differ by a mean absolute deviation of ~ 12 kJ/mol from the experimental dissociation barriers. The offset of 45 kJ/mol does not affect the prediction of relative affinities and may be an estimate of the heme- and protein-specific contribution to the oxygen affinity beyond the distal effect (proximal His conformation, heme side chains, and protein electrostatics in sperm whale myoglobin). If the WT H64 is corrected for the free energy of binding water to the deoxy state, the correction would be much smaller than these effects (0.6 occupancy has been suggested, consistent with ~ 5 kJ/mol from the change in dissociation constant of water).¹³⁴ As we are interested in the general effects of distal modulation of O_2 binding, *ceteris paribus*, such specific protein effects must be considered separately for each protein class.

The O_2 affinity does not increase with shorter Fe–O bond length, as might otherwise be expected. This is due to the effect of hydrogen bonding in increasing Fe–O slightly ($+0.01$ Å) while at the same time stabilizing the overall structure of the O_2 adduct. In other words, whereas M–L bond lengths are normally inversely related to ligand L dissociation energies, this does not hold true when the ligand is stabilized differently by secondary interactions.

CONCLUSIONS

This paper has reported a systematic investigation of the impact of distal interactions on the electronic structure and spectroscopic properties of oxyheme. While the porphyrin ring itself and the proximal histidine contribute in several ways to optimize the relevant redox potentials, reorganization energies, and spin crossover proficiency of hemes,^{8,26,27,30} the present study quantifies how distal hydrogen bonding affects the previously identified^{25,114} $d \rightarrow \pi^*$ back-donation from iron to O_2 , the Fe–O and O–O bonds, spin densities, spectroscopic data, and thermodynamics of O_2 binding. As hydrogen bond donor strength increases from complete absence with hydrophobic groups, via weak bonds with water or Gln, to strong bonds with long, flexible, cationic hydrogen bond donors, changes in electronic structure (bond lengths and spin densities) occur that can be shown to correlate remarkably well with changes in vibration frequencies and isomer shifts of the hemes.

Among notable observations are the following:

(i) Side groups of the heme cause a withdrawal of electron density from iron resulting in a 0.06 mm/s reduction in isomer shift, which should be corrected for when using porphine models.

(ii) The distal hydrogen bond to O_2 can change the isomer shift by 0.05 mm/s, with stronger hydrogen bonding giving smaller isomer shifts suggesting increased Fe(III) character.

(iii) Hydrogen bond donation correlates with larger weight of the Weiss Fe(III)– O_2^- , as the partial positive charge lowers the energy of the π^* orbitals and increases the spin polarization and ionicity of the Fe–O bond, consistent with previous findings.¹³

(iv) This leads to increased back-donation into π^* (O–O bond activation), i.e., longer O–O bonds and lower O–O stretch vibrations that anticorrelate with bond length in the normal sense.

(v) As estimated from the O–O bonds, hydrogen bonding can change the superoxide component from ~58 to ~75%, consistent with previous CASSCF calculations giving roughly a half–half mixture of Weiss and Pauling-type configurations without distal interactions.¹¹⁵

(vi) At the same time, oxygen affinity increases by stabilizing bound O_2 .

(vii) While this spectrum of hydrogen bonding correlates also with higher Fe–O stretch vibrations, testifying to a stronger ionic Fe(III)– O_2^- bond (the Weiss component), it is poorly correlated or leads to longer Fe–O bonds. This counterintuitive effect is due to the hydrogen bonding pulling the entire O_2 while at the same time increasing back-donation and the Weiss component, stabilizing the Fe–O bond despite its elongation (i.e., the equilibrium distance increases but the gain in ionic bond strength more than compensates the longer bond distance).

(viii) The isomer shifts are shown to correlate well with this tendency, with a smaller shift indicating increased Weiss configuration, back-bonding, and O–O activation, in the same way as the O–O bond length or stretch vibration. Thus, among the identified correlations of this work, the substantial correlation between the isomer shift and the O–O bond length or stretch vibration are particularly prevalent and informative.

The observed relations between spectroscopic properties and their interpretation in terms of an ionic model of bonding may

be relevant in many cases and have several implications. For example, the tendency of hydrogen bonds to both activate the O–O bond and at the same time increase the O_2 affinity, reflected in lower O–O stretch vibrations and higher isomer shifts, can be understood as an increased ionic component of bonding, where electron density on O_2 is stabilized by the electron-withdrawing distal hydrogens. The changes in spectroscopic fingerprints should allow a distinction between strong hydrogen donors, such as Arg found in some hemoprotein variants, of possible diagnostic value. Also, activation of O–O achieved by many enzymes upon binding of O_2 may be facilitated by hydrogen bonds and could be monitored by both a lowering of O–O stretch frequency and isomer shift, whereas the Fe–O stretch would be coupled and a poor proxy of ligand activation. The correlations may thus also be of value in estimating the efficiency of O–O activating iron catalysts.

The balance between reversible O_2 storage, as seen in globins, and O–O activation, as seen in iron oxygenases, may depend critically on this ability of hydrogen bonds to tune back-donation. In this context, the remarkable molecular evolution of heme becomes even more fascinating via the central role that distal interactions play in tuning the electronic structure of heme O_2 . The vital tuning of K_{O_2} leads to optimal reversible binding of O_2 to myoglobin at physiological P_{O_2} of the muscle cells, to enhance O_2 delivery to the mitochondria by distinct storage or transport.¹³⁵ Using improved physiological models of the muscle cell with integrated P_{O_2} profiles, it can be shown directly how vital this distal tuning is for survival, as exemplified by the substantial reductions in dive times of marine mammals associated with mutating the E7 residue.¹³⁶ Considering the few variables involved in tuning the heme system, it is amazing that it produces such a diversity of chemical qualities, e.g., small redox potentials, small reorganization energies, and small spin crossover energies, all somehow relevant to the handling of O_2 during oxidative metabolism. It is our hope that the present account of the interplay between distal effects, electronic structure, spectroscopy, and O_2 binding to heme will be of value in future research into iron– O_2 systems.

ASSOCIATED CONTENT

Supporting Information

Part I, Mössbauer calculations and validation data set; part II, properties and electronic energies for heme models; part III, analysis of structure–property correlations; part IV, structural coordinates of key optimized heme models. This material is available free of charge via the Internet at <http://pubs.acs.org>.

AUTHOR INFORMATION

Corresponding Author

*E-mail: kpj@kemi.dtu.dk. Phone: +045 45 25 24 09.

Notes

The authors declare no competing financial interest.

ACKNOWLEDGMENTS

The authors acknowledge the Danish Center for Scientific Computing (DCSC) for providing a computing grant (Grant 2012-02-23).

REFERENCES

- (1) Tezcan, F. A.; Winkler, J. R.; Gray, H. B. Effects of Ligation and Folding on Reduction Potentials of Heme Proteins. *J. Am. Chem. Soc.* **1998**, *120*, 13383–13388.
- (2) Olea, C., Jr.; Kuriyan, J.; Marletta, M. A. Modulating Heme Redox Potential through Protein-Induced Porphyrin Distortion. *J. Am. Chem. Soc.* **2010**, *132*, 12794–12795.
- (3) Voigt, P.; Knapp, E. W. Tuning Heme Redox Potentials in the Cytochrome *c* Subunit of Photosynthetic Reaction Centers. *J. Biol. Chem.* **2003**, *278*, 51993–52001.
- (4) Cowley, A. B.; Kennedy, M. L.; Silchenko, S.; Lukat-Rodgers, G. S.; Rodgers, K. R.; Benson, D. R. Insight into Heme Protein Redox Potential Control and Functional Aspects of Six-Coordinate Ligand-Sensing Heme Proteins From Studies of Synthetic Heme Peptides. *Inorg. Chem.* **2006**, *45*, 9985–10001.
- (5) Battistuzzi, G.; Bellei, M.; Bortolotti, C. A.; Sola, M. Redox Properties of Heme Peroxidases. *Arch. Biochem. Biophys.* **2010**, *500*, 21–36.
- (6) Rydberg, P.; Sigfridsson, E.; Ryde, U. On the Role of the Axial Ligand in Heme Proteins: A Theoretical Study. *J. Biol. Inorg. Chem.* **2004**, *9*, 203–223.
- (7) Zámocký, M.; Furtmüller, P. G.; Obinger, C. Evolution of Structure and Function of Class I Peroxidases. *Arch. Biochem. Biophys.* **2010**, *500*, 45–57.
- (8) Jensen, K. P.; Ryde, U. Comparison of the Chemical Properties of Iron and Cobalt Porphyrins and Corrins. *ChemBioChem* **2003**, *4*, 413–424.
- (9) Sigfridsson, E.; Olsson, M. H. M.; Ryde, U. A Comparison of the Inner-Sphere Reorganization Energies of Cytochromes, Iron–Sulfur Clusters, and Blue Copper Proteins. *J. Phys. Chem. B* **2001**, *105*, 5546–5552.
- (10) Tsuda, M.; Dy, E. S.; Kasai, H. Comparative Study of O₂ Dissociation on Various Metalloporphyrins. *J. Chem. Phys.* **2005**, *233*, 244719.
- (11) Sanders, L. K.; Arnold, W. D.; Oldfield, E. NMR, IR, Mössbauer and Quantum Chemical Investigations of Metalloporphyrins and Metalloproteins. *J. Porphyrins Phthalocyanines* **2001**, *5*, 323–333.
- (12) Unno, M.; Chen, H.; Kusama, S.; Shaik, S.; Ikeda-Saito, M. Structural Characterization of the Fleeting Ferric Peroxo Species in Myoglobin: Experiment and Theory. *J. Am. Chem. Soc.* **2007**, *129*, 13394–13395.
- (13) Chen, H.; Ikeda-Saito, M.; Shaik, S. Nature of The Fe–O₂ Bonding in Oxy-Myoglobin: Effect of the Protein. *J. Am. Chem. Soc.* **2008**, *130*, 14778–14790.
- (14) Blomberg, L. M.; Blomberg, M. R. A.; Siegbahn, P. E. M. A Theoretical Study on the Binding of O₂, NO and CO to Heme Proteins. *J. Inorg. Biochem.* **2005**, *99*, 949–958.
- (15) Rovira, C.; Kunc, K.; Hutter, J.; Ballone, P.; Parrinello, M. Equilibrium Geometries and Electronic Structure of Iron–Porphyrin Complexes: A Density Functional Study. *J. Phys. Chem. A* **1997**, *101*, 8914–8925.
- (16) Liao, M.-S.; Huang, M.-J.; Watts, J. D. FeP(Im)-AB Bonding Energies Evaluated with a Large Number of Density Functionals (P = Porphine, Im = Imidazole, AB = CO, NO, and O₂). *Mol. Phys.* **2011**, *109*, 2035–2048.
- (17) Sigfridsson, E.; Ryde, U. On the Significance of Hydrogen Bonds for the Discrimination between CO and O₂ by Myoglobin. *J. Biol. Inorg. Chem.* **1999**, *4*, 99–110.
- (18) De Angelis, F.; Car, R.; Spiro, T. G. Role of Ligand Bending in the Photodissociation of O₂ Vs CO-Heme: A Time-Dependent Density Functional Study. *J. Am. Chem. Soc.* **2003**, *125*, 15710–15711.
- (19) Kaupp, M.; Rovira, C.; Parrinello, M. Density Functional Study of ¹⁷O NMR Chemical Shift and Nuclear Quadrupole Coupling Tensors in Oxyheme Model Complexes. *J. Phys. Chem. B* **2000**, *104*, 5200–5208.
- (20) Radoń, M.; Pierloot, K. Binding of CO, NO, and O₂ to Heme by Density Functional and Multireference Ab Initio Calculations. *J. Phys. Chem. A* **2008**, *112*, 11824–11832.
- (21) Barea, G.; Maseras, F.; Lledos, A. Unexpectedly Large Basis Set Effects on the Binding of O₂ to Heme Complexes. *Int. J. Quantum Chem.* **2001**, *85*, 100–108.
- (22) Siegbahn, P. E. M.; Blomberg, M. R. A.; Chen, S.-L. Significant van der Waals Effects in Transition Metal Complexes. *J. Chem. Theory Comput.* **2010**, *6*, 2040–2044.
- (23) Li, J.; Peng, Q.; Barabanschikov, A.; Pavlik, J. W.; Alp, E. E.; Sturhahn, W.; Zhao, J.; Schulz, C. E.; Sage, J. T.; Scheidt, W. R. New Perspectives on Iron-Ligand Vibrations of Oxyheme Complexes. *Chem.—Eur. J.* **2011**, *17*, 11178–11185.
- (24) Liu, Y.; Sun, H. Electronic Ground States and Vibrational Frequency Shifts of Diatomic Ligands in Heme Adducts. *J. Comput. Chem.* **2011**, *32*, 1279–1285.
- (25) Vogel, K. M.; Kozłowski, P. M.; Zgierski, M. Z.; Spiro, T. G. General Solid-Phase Method for the Preparation of Mechanism-Based Cysteine Protease Inhibitors. *J. Am. Chem. Soc.* **1999**, *121*, 9915–9921.
- (26) Jensen, K. P.; Ryde, U. Comparison of Chemical Properties of Iron, Cobalt, and Nickel Porphyrins, Corrins, and Hydrocorphins. *J. Porphyrins Phthalocyanines* **2005**, *9*, 581–606.
- (27) Jensen, K. P.; Ryde, U. Importance of Proximal Hydrogen Bonds in Haem Proteins. *Mol. Phys.* **2003**, *101*, 2003–2018.
- (28) Landau, L. Zur Theorie der Energieübertragung. II. *Phys. Sov. Union* **1932**, *2*, 46–51.
- (29) Zener, C. Non-adiabatic Crossing of Energy Levels. *Proc. R. Soc. A* **1932**, *137*, 696–702.
- (30) Jensen, K. P.; Ryde, U. How O₂ Binds to Heme: Reasons for Rapid Binding and Spin Inversion. *J. Biol. Chem.* **2004**, *279*, 14561–14569.
- (31) Olson, J. S.; Phillips, G. N., Jr. Myoglobin Discriminates Between O₂, NO, and CO by Electrostatic Interactions with the Bound Ligand. *J. Biol. Inorg. Chem.* **1997**, *2*, 544–552.
- (32) Springer, B. A.; Sligar, S. G.; Olson, J. S.; Phillips, G. N., Jr. Mechanisms of Ligand Recognition in Myoglobin. *Chem. Rev.* **1994**, *94*, 699–714.
- (33) Momenteau, M.; Reed, C. A. Synthetic Heme Dioxygen Complexes. *Chem. Rev.* **1994**, *94*, 659–698.
- (34) Marti, M. A.; Crespo, A.; Capece, L.; Boechi, L.; Bikiel, D. E.; Scherlis, D. A.; Estrin, D. A. Dioxygen Affinity in Heme Proteins Investigated by Computer Simulation. *J. Inorg. Biochem.* **2005**, *100*, 761–770.
- (35) Das, T. D.; Couture, M.; Ouellet, Y.; Guertin, M.; Rousseau, D. L. Simultaneous Observation of the O—O and Fe—O₂ Stretching Modes in Oxyhemoglobins. *Proc. Natl. Acad. Sci. U.S.A.* **2001**, *98*, 479–484.
- (36) Jensen, K. P.; Cirera, J. Accurate Computed Enthalpies of Spin Crossover in Iron and Cobalt Complexes. *J. Phys. Chem. A* **2009**, *113*, 10033–10039.
- (37) Kepp, K. P. The Ground States of Iron(III) Porphines: Role of Entropy-Enthalpy Compensation, Fermi Correlation, Dispersion, and Zero-Point Energies. *J. Inorg. Biochem.* **2011**, *105*, 1286–1292.
- (38) Furche, F.; Perdew, J. P. The Performance of Semilocal and Hybrid Density Functionals in 3d Transition-Metal Chemistry. *J. Chem. Phys.* **2006**, *124*, 044103.
- (39) Zhao, Y.; Truhlar, D. G. Comparative Assessment of Density Functional Methods for 3d Transition-Metal Chemistry. *J. Chem. Phys.* **2006**, *124*, 224105.
- (40) Jensen, K. P. Bioinorganic Chemistry Modeled with the TPSSH Density Functional. *Inorg. Chem.* **2008**, *47*, 10357–10365.
- (41) Jensen, K. P. Metal-Ligand Bonds of Second- and Third-Row D-Block Metals Characterized by Density Functional Theory. *J. Phys. Chem. A* **2009**, *113*, 10133–10141.
- (42) Geerlings, P.; De Proft, F.; Langenaeker, W. Conceptual Density Functional Theory. *Chem. Rev.* **2003**, *103*, 1793–1873.
- (43) Kohn, W.; Becke, A. D.; Parr, R. G. Density Functional Theory of Electronic Structure. *J. Phys. Chem.* **1996**, *100*, 12974–12980.
- (44) Parr, R. G.; Yang, W. *Density Functional Theory of Atoms and Molecules*; Oxford University Press: New York, 1989.

- (45) Harvey, J. N. On the Accuracy of Density Functional Theory in Transition Metal Chemistry. *Annu. Rep. Prog. Chem., Sect. C* **2006**, *102*, 203–226.
- (46) Zhao, Y.; Truhlar, D. G. Density Functionals with Broad Applicability in Chemistry. *Acc. Chem. Res.* **2008**, *41*, 157–167.
- (47) Becke, A. D. Becke's Three Parameter Hybrid Method Using the LYP Correlation Functional. *J. Chem. Phys.* **1993**, *98*, 5648–5652.
- (48) Siegbahn, P. E. M. The Performance of Hybrid DFT for Mechanisms Involving Transition Metal Complexes in Enzymes. *J. Biol. Inorg. Chem.* **2006**, *11*, 695–701.
- (49) Kepp, K. P. Consistent Descriptions of Metal–Ligand Bonds and Spin-Crossover in Inorganic Chemistry. *Coord. Chem. Rev.* **2013**, *257*, 196–209.
- (50) Handy, N. C.; Cohen, A. Left–Right Correlation Energy. *J. Mol. Phys.* **2001**, *99*, 403–412.
- (51) Lee, C.; Yang, W.; Parr, R. G. Development of the Colle-Salvetti Correlation-Energy Formula into a Functional of the Electron Density. *Phys. Rev. B* **1988**, *37*, 785–789.
- (52) Grimme, S. Semiempirical Hybrid Density Functional with Perturbative Second-Order Correlation. *J. Chem. Phys.* **2006**, *124*, 034108.
- (53) Tao, J.; Perdew, J. P.; Staroverov, V. N.; Scuseria, G. E. Climbing the Density Functional Ladder: Nonempirical Meta-Generalized Gradient Approximation Designed for Molecules and Solids. *Phys. Rev. Lett.* **2003**, *91*, 146401.
- (54) Perdew, J. P.; Tao, J.; Staroverov, V. N.; Scuseria, G. E. Meta-Generalized Gradient Approximation: Explanation of a Realistic Nonempirical Density Functional. *J. Chem. Phys.* **2004**, *120*, 6898–6911.
- (55) Becke, A. D. Density-Functional Exchange-Energy Approximation with Correct Asymptotic Behavior. *Phys. Rev. A* **1988**, *38*, 3098–3100.
- (56) Perdew, J. P. Density-Functional Approximation for the Correlation Energy of the Inhomogeneous Electron Gas. *Phys. Rev. B* **1986**, *33*, 8822–8824.
- (57) Reiher, M. Theoretical Study of the Fe(Phen)₂(NCS)₂ Spin-Crossover Complex with Reparametrized Density Functionals. *Inorg. Chem.* **2002**, *41*, 6928–6935.
- (58) Daku, L. M. L.; Vargas, A.; Hauser, A.; Fouqueau, A.; Casida, M. E. Assessment of Density Functionals for the High-Spin/Low-Spin Energy Difference in the Low-Spin Iron(II) Tris(2,2'-Bipyridine) Complex. *ChemPhysChem* **2005**, *6*, 1393–1410.
- (59) Zein, S.; Borshch, S. A.; Fleurat-Lessard, P.; Casida, M. E.; Chermette, H. Assessment of the Exchange-Correlation Functionals for the Physical Description of Spin Transition Phenomena by Density Functional Theory Methods: All The Same? *J. Chem. Phys.* **2007**, *126*, 014105.
- (60) Hughes, T. F.; Friesner, R. A. Correcting Systematic Errors in DFT Spin-Splitting Energetics for Transition Metal Complexes. *J. Chem. Theory Comput.* **2011**, *7*, 19–32.
- (61) Jensen, K. P.; Roos, B. O.; Ryde, U. Performance of Density Functionals for First Row Transition Metal Systems. *J. Chem. Phys.* **2007**, *126*, 014103.
- (62) Staroverov, V. N.; Scuseria, G. E.; Tao, J.; Perdew, J. P. Comparative assessment of a new nonempirical density functional: Molecules and hydrogen-bonded complexes. *J. Chem. Phys.* **2003**, *119*, 12129–12137.
- (63) Rydberg, P.; Olsen, L. The Accuracy of Geometries for Iron Porphyrin Complexes from Density Functional Theory. *J. Phys. Chem. A* **2009**, *113*, 11949–11953.
- (64) Conradie, M. M.; Conradie, J.; Ghosh, A. Capturing The Spin State Diversity of Iron(III)-Aryl Porphyrins: OLYP Is Better than TPSSH. *J. Inorg. Biochem.* **2011**, *105*, 84–91.
- (65) Ye, S.; Neese, F. Accurate Modeling of Spin-State Energetics in Spin-Crossover Systems with Modern Density Functional Theory. *Inorg. Chem.* **2010**, *49*, 772–774.
- (66) Turner, J. W.; Schultz, F. A. Coupled Electron-Transfer and Spin-Exchange Reactions. *Coord. Chem. Rev.* **2001**, *219–221*, 81–97.
- (67) Paulsen, H.; Trautwein, A. X. Density Functional Theory Calculations for Spin Crossover Complexes. *Top. Curr. Chem.* **2004**, *235*, 197–219.
- (68) Cirera, J.; Paesani, F. Theoretical Prediction of Spin-Crossover Temperatures in Ligand-Driven Light-Induced Spin Change Systems. *Inorg. Chem.* **2012**, *51*, 8194–8201.
- (69) Orio, M.; Pantazis, D. A.; Petrenko, T.; Neese, F. Magnetic and Spectroscopic Properties of Mixed Valence Manganese(III,IV) Dimers: A Systematic Study Using Broken Symmetry Density Functional Theory. *Inorg. Chem.* **2009**, *48*, 7251–7260.
- (70) Pantazis, D. A.; Orio, M.; Petrenko, T.; Zein, S.; Bill, E.; Lubitz, W.; Messinger, J.; Neese, F. A New Quantum Chemical Approach to the Magnetic Properties of Oligonuclear Transition-Metal Complexes: Application to a Model for the Tetranuclear Manganese Cluster of Photosystem II. *J. Chem.—Eur. J.* **2009**, *15*, 5108–5123.
- (71) Grimme, S.; Antony, J.; Ehrlich, S.; Krieg, H. A Consistent and Accurate ab Initio Parametrization of Density Functional Dispersion Correction (DFT-D) for the 94 Elements H–Pu. *J. Chem. Phys.* **2010**, *132*, 154104.
- (72) Kang, R.; Chen, H.; Shaik, S.; Yao, J. *J. Chem. Theory Comput.* **2011**, *7*, 4002–4011.
- (73) Ahlrichs, R.; Bär, M.; Häser, M.; Horn, H.; Kölmel, C. Electronic Structure Calculations on Workstation Computers: The Program System Turbomole. *Chem. Phys. Lett.* **1989**, *162*, 165–169.
- (74) Klamt, A.; Jonas, V.; Bürger, T.; Lohrenz, J. C. W. Refinement and Parametrization of COSMO-RS. *J. Phys. Chem. A* **1998**, *102*, 5074–5085.
- (75) Weigend, F.; Ahlrichs, R. Balanced Basis Sets of Split Valence, Triple Zeta Valence and Quadruple Zeta Valence Quality for H to Rn: Design And Assessment of Accuracy. *Phys. Chem. Chem. Phys.* **2005**, *7*, 3297–3305.
- (76) Vojtechovský, J.; Chu, K.; Berendzen, J.; Sweet, R. M.; Schlichting, I. Crystal Structures of Myoglobin-Ligand Complexes at Near-Atomic Resolution. *Biophys. J.* **1999**, *77*, 2153–2174.
- (77) ArgusLab, version 4.01; Mark Thompson and Planaria Software LLC, 2004.
- (78) Goldbeck, R. A.; Bhaskaran, S.; Ortega, C.; Mendoza, J. L.; Olson, J. S.; Soman, J.; Kliger, D. S.; Esquerra, R. M. Water and Ligand Entry in Myoglobin: Assessing the Speed and Extent of Heme Pocket Hydration after CO Photodissociation. *Proc. Natl. Acad. Sci. U.S.A.* **2006**, *103*, 1254–1259.
- (79) Schafer, A.; Horn, H.; Ahlrichs, R. Fully Optimized Contracted Gaussian Basis Sets for Atoms Li to Kr. *J. Chem. Phys.* **1992**, *97*, 2571–2577.
- (80) Andrade, S. G.; Gonçalves, L. C. S.; Jorge, F. E. Scaling Factors for Fundamental Vibrational Frequencies and Zero-Point Energies Obtained from HF, MP2, and DFT/DZP and TZP Harmonic Frequencies. *J. Mol. Struct.: THEOCHEM* **2008**, *864*, 20–25.
- (81) Liu, T.; Lovell, T.; Han, W. G.; Noodleman, L. DFT Calculations of Isomer Shifts and Quadrupole Splitting Parameters in Synthetic Iron-Oxo Complexes: Applications to Methane Monooxygenase and Ribonucleotide Reductase. *Inorg. Chem.* **2003**, *42*, 5244–5251.
- (82) Marathe, V. R.; Trautwein, A. X. In *Advances in Mössbauer Spectroscopy*; Thosar, B. V., Srivasta, J. K., Iyengar, P. K., Bhargava, S. C., Eds.; Elsevier: Amsterdam, 1985.
- (83) Reschke, R.; Trautwein, A. X. Electronic Structure, Pressure- and Temperature-Dependent Charge Densities, and Electric Field Gradients in Fe₂. *Phys. Rev. B* **1977**, *15*, 2708–2717.
- (84) Lovell, T.; Li, J.; Liu, T.; Case, D. A.; Noodleman, L. FeMo Cofactor of Nitrogenase: A Density Functional Study of States M(N), M(OX), M(R), and M(I). *J. Am. Chem. Soc.* **2001**, *123*, 12392–12410.
- (85) Zhang, Y.; Mao, J.; Oldfield, E. ⁵⁷Fe Mössbauer Isomer Shifts of Heme Protein Model Systems: Electronic Structure Calculations. *J. Am. Chem. Soc.* **2002**, *124*, 7829–7839.
- (86) Neese, F. Prediction and Interpretation of Isomer Shifts in ⁵⁷Fe Mössbauer Spectra by Density Functional Theory. *Inorg. Chim. Acta* **2002**, *337*, 181–192.

- (87) Filatov, M. First Principles Calculation of Mössbauer Isomer Shift. *Coord. Chem. Rev.* **2009**, *253*, 594–605.
- (88) Nemykin, V. N.; Hadt, R. G. Influence of Hartree-Fock Exchange on the Calculated Mössbauer Isomer Shifts and Quadrupole Splittings in Ferrocene Derivatives Using Density Functional Theory. *Inorg. Chem.* **2006**, *45*, 8297–8307.
- (89) Freeman, A. J.; Ellis, D. In *Mössbauer Isomer Shifts*; Shenoy, G. K., Wagner, F. E., Eds.; North-Holland: Amsterdam, 1978; p 111.
- (90) Shirley, D. A. Application and Interpretation of Isomer Shifts. *Rev. Mod. Phys.* **1964**, *36*, 339–351.
- (91) Bohle, D. S.; Debrunner, P.; Fitzgerald, J. P.; Hansert, B.; Hung, C.-H.; Thomson, A. J. Electronic Origin of Variable Denitrosylation Kinetics from Isostructural $[\text{Fe}(\text{NO})]^7$ Complexes: X-ray Crystal Structure of $[\text{Fe}(\text{oetap})(\text{NO})]$. *Chem. Commun.* **1997**, 91–92.
- (92) Witten, E. H.; Reiff, W. M.; Lazar, K.; Sullivan, B. W.; Foxman, B. M. The Ferric Chloride- α -diamine System. 3. X-ray Crystallographic, Magnetic Susceptibility, and Zero- and High-Field Mössbauer Spectroscopy Investigation of Bis(2,2'-bipyridine)dichloroiron-(2+) tetrachloroferrate(2-): Slow Paramagnetic Relaxation and Magnetic Ordering of Complex Bimetallic Salts. *Inorg. Chem.* **1985**, *24*, 4585–4591.
- (93) Vogel, E.; Will, S.; Tilling, A. S.; Neumann, L.; Lex, J.; Bill, E.; Trautwein, A. X.; Wieghardt, K. Metalloporphyrins with Formally Tetravalent Iron. *Angew. Chem., Int. Ed. Engl.* **1994**, *33*, 731–735.
- (94) Vincent, J. B.; Huffman, J. C.; Christou, G.; Li, Q.; Nanny, M. A.; Hendrickson, D. N.; Fong, R. H.; Fish, R. H. Modeling the Dinuclear Sites of Iron Biomolecules: Synthesis and Properties of $\text{Fe}_2\text{O}(\text{OAc})_2\text{Cl}_2(\text{bipy})_2$ and Its Use as an Alkane Activation Catalyst. *J. Am. Chem. Soc.* **1988**, *110*, 6898–6900.
- (95) Kerler, W.; Neuwirth, W.; Fluck, E. Untersuchung Komplexer und Kovalenter Eisenverbindungen mit Hilfe des Mössbauer-Effekts von Fe^5 . *Z. Phys.* **1963**, *175*, 200–220.
- (96) Debrunner, P. G. In *Iron Porphyrins*; Lever, A. B. P., Gray, H. B., Eds.; VCH Publishers: New York, 1989; Vol. 3, pp 139–234.
- (97) Wertheim, G. K.; Buchanan, D. N. E. Temperature Dependence of the Fe^{57} hfs in FeF_2 below the Néel Temperature. *Phys. Rev.* **1967**, *161*, 478–482.
- (98) Nieuwport, W. C.; Post, D.; Van Duijnen, P. T. Calibration Constant for ^{57}Fe Mössbauer Isomer Shifts Derived from ab Initio Self-Consistent-Field Calculations on Octahedral FeF_6 and $\text{Fe}(\text{CN})_6$ Clusters. *Phys. Rev. B* **1978**, *17*, 91–98.
- (99) Havlin, R. H.; Godbout, N.; Salzmann, R.; Wojdelski, M.; Arnold, W.; Schulz, C. E.; Oldfield, E. An Experimental and Density Functional Theoretical Investigation of Iron-57 Mössbauer Quadrupole Splittings in Organometallic and Heme-Model Compounds: Applications to Carbonmonoxyheme Protein Structure. *J. Am. Chem. Soc.* **1998**, *120*, 3144–3151.
- (100) Han, W. G.; Liu, T. Q.; Lovell, T.; Noodleman, L. DFT Calculations of ^{57}Fe Mössbauer Isomer Shifts and Quadrupole Splittings for Iron Complexes in Polar Dielectric Media: Applications to Methane Monooxygenase and Ribonucleotide Reductase. *J. Comput. Chem.* **2006**, *27*, 1292–1306.
- (101) Dunlap, R. A.; Stroink, G. Temperature Dependence of the ^{57}Fe Mössbauer Effect Parameters for Amorphous $\text{Fe}_{73}\text{Mo}_7\text{B}_{20}$. *J. Phys. F: Met. Phys.* **1984**, *14*, 3083–3091.
- (102) Dolphin, D.; Sams, J. R.; Tsien, T. B.; Wong, K. L. Synthesis and Mössbauer Spectra of Octaethylporphyrin Ferrous Complexes. *J. Am. Chem. Soc.* **1976**, *98*, 6970–6975.
- (103) Kent, T. A.; Spartalian, K.; Lang, G.; Yonetani, T.; Reed, C. A.; Collman, J. P. High Magnetic Field Mössbauer Studies of Deoxymyoglobin, Deoxyhemoglobin, and Synthetic Analogues. *Biochim. Biophys. Acta* **1979**, *580*, 245–258.
- (104) Stephens, P. J.; Devlin, F. J.; Chabalowski, C. F.; Frisch, M. J. Ab Initio Calculation of Vibrational Absorption and Circular Dichroism Spectra Using Density Functional Force Fields. *J. Phys. Chem.* **1994**, *98*, 11623–11627.
- (105) Srivastava, T. S.; Tyagi, S.; Nath, A. Emission Mössbauer Study of the Stereochemical Trigger that Initiates Cooperative Interaction of Hemoglobin Subunits. *Proc. Natl. Acad. Sci. U.S.A.* **1977**, *74*, 4996–5000.
- (106) Oshtrakh, M. I.; Kumar, A.; Kundu, S.; Berkovsky, A. L.; Semionkin, V. A. Study of Human, Rabbit and Pig Oxyhemoglobins Using High Velocity Resolution Mössbauer Spectroscopy in Relation to their Structural and Functional Variations. *J. Mol. Struct.: THEOCHEM* **2011**, *993*, 292–296.
- (107) Oshtrakh, M. I.; Berkovsky, A. L.; Kumar, A.; Kundu, S.; Vinogradov, A. V.; Konstantinova, T. S.; Semionkin, V. A. Heme Iron State in Various Oxyhemoglobins Probed Using Mössbauer Spectroscopy with a High Velocity Resolution. *Biometals* **2011**, *24*, 501–512.
- (108) Marchant, L.; Sharrock, M.; Hoffman, B. M.; Münck, E. Study of an Oxygenated Heme Complex in Frozen Solution by Mössbauer Emission Spectroscopy. *Proc. Natl. Acad. Sci. U.S.A.* **1972**, *69*, 2396–2399.
- (109) Hu, C.; Roth, A.; Ellison, M. K.; An, J.; Ellis, C. M.; Schulz, C. E.; Scheidt, W. R. Electronic Configuration Assignment and the Importance of Low-Lying Excited States in High-Spin Imidazole-Ligated Iron(II) Porphyrins. *J. Am. Chem. Soc.* **2005**, *127*, 5675–5688.
- (110) Cruickshank, D. W. Remarks about Protein Structure Precision. *Acta Crystallogr.* **1999**, *D55*, 583–601.
- (111) Sommerhalter, M.; Lieberman, R. L.; Rosenzweig, A. C. X-Ray Crystallography and Biological Metal Centers: Is Seeing Believing? *Inorg. Chem.* **2005**, *44*, 770–778.
- (112) Ryde, U.; Nilsson, K. Quantum Chemistry Can Locally Improve Protein Crystal Structures. *J. Am. Chem. Soc.* **2003**, *125*, 14232–14233.
- (113) Ryde, U.; Nilsson, K. Quantum Refinement—A Combination of Quantum Chemistry and Protein Crystallography. *J. Mol. Struct.: THEOCHEM* **2003**, *632*, 259–275.
- (114) Li, X.-Y.; Spiro, T. G. Is Bound Carbonyl Linear or Bent in Heme Proteins? Evidence from Resonance Raman and Infrared Spectroscopic Data. *J. Am. Chem. Soc.* **1988**, *110*, 6024–6033.
- (115) Jensen, K. P.; Roos, B. O.; Ryde, U. O_2 -Binding to Heme: Electronic Structure and Spectrum of Oxyheme, Studied by Multi-configurational Methods. *J. Inorg. Biochem.* **2005**, *99*, 978.
- (116) Pauling, L.; Coryell, C. D. The Magnetic Properties and Structure of Hemoglobin, Oxyhemoglobin and Carbonmonoxyhemoglobin. *Proc. Natl. Acad. Sci. U.S.A.* **1936**, *22*, 210–216.
- (117) Yu, N. T.; Thompson, H. M.; Chang, C. K. Resonance Raman Studies of Dioxygen and Carbon Monoxide Binding to Imidazole-Appended Hemes. *Biophys. J.* **1987**, *51*, 283–287.
- (118) Collman, J. P.; Brauman, J. I.; Halbert, T. R.; Suslick, K. S. Nature of O_2 and CO Binding to Metalloporphyrins and Heme Proteins. *Proc. Natl. Acad. Sci. U.S.A.* **1976**, *73*, 3333–3337.
- (119) Maxwell, J. C.; Volpe, J. A.; Barlow, C. H.; Caughey, W. S. Infrared Evidence for the Mode of Binding of Oxygen to Iron of Myoglobin from Heart Muscle. *Biochem. Biophys. Res. Commun.* **1974**, *58*, 166–171.
- (120) Weiss, J. J. Nature of the Iron-Oxygen Bond in Oxyhaemoglobin. *Nature* **1964**, *202*, 83–84.
- (121) Pauling, L. The Interpretation of Some Chemical Properties of Hemoglobin in Terms of Its Molecular Structure. *Stanford Med. Bull.* **1948**, *6*, 215–217.
- (122) Pauling, L. Nature of the Iron–Oxygen Bond in Oxyhaemoglobin. *Nature* **1964**, *203*, 182–183.
- (123) McClure, D. S. Electronic Structure of Transition Metal Complex Ions. *Radiat. Res. Suppl.* **1960**, *2*, 218–242.
- (124) Goddard, W. A.; Olafson, B. D. Ozone Model for Bonding of an O_2 to Heme in Oxyhemoglobin. *Proc. Natl. Acad. Sci. U.S.A.* **1975**, *72*, 2335–2339.
- (125) Olafson, B. D.; Goddard, W. A. Molecular Description of Dioxygen Bonding in Hemoglobin. *Proc. Natl. Acad. Sci. U.S.A.* **1977**, *74*, 1315–1319.
- (126) Tucker, P. W.; Phillips, S. E.; Perutz, M. F.; Houtchens, R.; Caughey, W. S. Molecular Description of Dioxygen Bonding in Hemoglobin. *Proc. Natl. Acad. Sci. U.S.A.* **1978**, *75*, 1076–1080.

- (127) Lacan, P.; Francina, A.; Souillet, G.; Aubry, M.; Couprie, N.; Dementhon, L.; Becchi, M. Two New α Chain Variants: Hb Boghé [$\alpha 58(\text{E7})\text{His} \rightarrow \text{Gln}$, $\alpha 2$], a Variant on the Distal Histidine, and Hb Charolles [$\alpha 103(\text{G10})\text{His} \rightarrow \text{Tyr}$, $\alpha 1$]. *Hemoglobin* **1999**, *23*, 345–352.
- (128) Scott, E. E.; Gibson, Q. H.; Olson, J. S. Mapping the Pathways for O_2 Entry Into and Exit from Myoglobin. *J. Biol. Chem.* **2001**, *276*, 5177–5188.
- (129) Mintz, C.; Clark, M.; Acree, W. E.; Abraham, M. H. Enthalpy of Solvation Correlations for Gaseous Solutes Dissolved in Water and in 1-Octanol Based on the Abraham Model. *J. Chem. Inf. Model.* **2007**, *47*, 115–121.
- (130) Graziano, G. On the Temperature Dependence of Hydration Thermodynamics for Noble Gases. *Phys. Chem. Chem. Phys.* **1999**, *1*, 1877–1886.
- (131) Lazaridis, T.; Paulaitis, M. E. Simulation Studies of the Hydration Entropy of Simple, Hydrophobic Solutes. *J. Phys. Chem.* **1994**, *98*, 635–642.
- (132) Ostermann, A.; Waschipky, R.; Parak, F. G.; Nienhaus, G. U. Ligand Binding and Conformational Motions in Myoglobin. *Nature* **2000**, *404*, 205–208.
- (133) Cohen, J.; Arkhipov, A.; Braun, R.; Schulten, K. Imaging the Migration Pathways for O_2 , CO, NO, and Xe Inside Myoglobin. *Biophys. J.* **2006**, *91*, 1844–1857.
- (134) Kachalova, G. S.; Popov, A. N.; Bartunik, H. D. A Steric Mechanism for Inhibition of CO Binding to Heme Proteins. *Science* **1999**, *284*, 473–476.
- (135) Dasmeh, P.; Kepp, K. P. Bridging the Gap Between Chemistry, Physiology, and Evolution: Quantifying the Functionality of Sperm Whale Myoglobin Mutants. *Comp. Biochem. Physiol., Part A* **2012**, *161*, 9–17.
- (136) Dasmeh, D.; Davis, R. W.; Kepp, K. P. Aerobic Dive Limits of Seals with Mutant Myoglobin Using Combined Thermochemical and Physiological Data. *Comp. Biochem. Physiol., Part A* **2013**, *164*, 119–128.